remote sensing

MDPI

Article

Estimation of Aerosol Layer Height from OLCI Measurements in the O_2A-Absorption Band over Oceans

Lena Katharina Jänicke *, Rene Preusker, Nicole Docter and Jürgen Fischer

Institute of Meteorology, Freie Universität Berlin (FUB), Carl-Heinrich-Becker-Weg 6-10, 12165 Berlin, Germany; rene.preusker@fu-berlin.de (R.P.); nicole.docter@wew.fu-berlin.de (N.D.); juergen.fischer@fu-berlin.de (J.F.)
* Correspondence: lena.jaenicke@wew.fu-berlin.de

Abstract: The aerosol layer height (ALH) is an important parameter that characterizes aerosol interaction with the environment. An estimation of the vertical distribution of aerosol is necessary for studies of those interactions, their effect on radiance and for aerosol transport models. ALH can be retrieved from satellite-based radiance measurements within the oxygen absorption band between 760 and 770 nm (O_2A band). The oxygen absorption is reduced when light is scattered by an elevated aerosol layer. The Ocean and Land Colour Imager (OLCI) has three bands within the oxygen absorption band. We show a congruent sensitivity study with respect to ALH for dust and smoke cases over oceans. Furthermore, we developed a retrieval of the ALH for those cases and an uncertainty estimation by applying linear uncertainty propagation and a bootstrap method. The sensitivity study and the uncertainty estimation are based on radiative transfer simulations. The impact of ALH, aerosol optical thickness (AOT), the surface roughness (wind speed) and the central wavelength on the top of atmosphere (TOA) radiance is discussed. The OLCI bands are sufficiently sensitive to ALH for cases with AOTs larger than 0.5 under the assumption of a known aerosol type. With an accurate spectral characterization of the OLCI O_2A bands better than 0.1 nm, ALH can be retrieved with an uncertainty of a few hundred meters. The retrieval of ALH was applied successfully on an OLCI dust and smoke scene. The found ALH is similar to parallel measurements by the Tropospheric Monitoring Instrument (TROPOMI). OLCI's high spatial resolution and coverage allow a detailed overview of the vertical aerosol distribution over oceans.

Keywords: aerosol layer height; O_2 absorption; OLCI; radiative transfer; sensitivity study

Citation: Jänicke, L.K.; Preusker, R.; Docter, N.; Fischer, J. Estimation of Aerosol Layer Height from OLCI Measurements in the O_2A-Absorption Band over Oceans. *Remote Sens.* **2023**, *15*, 4080. https://doi.org/10.3390/rs15164080

Academic Editors: Craig Donlon, Peter North and Alexander Kokhanovsky

Received: 3 July 2023
Revised: 14 August 2023
Accepted: 16 August 2023
Published: 18 August 2023

1. Introduction

Aerosol is a mixture of particulate matter in the atmosphere with natural or anthropogenic origin. Depending on its origin, aerosol can be distributed differently within the atmosphere. For example, industrial aerosol is rather found within the boundary layer, soil from a dust outbreak of a desert can be transported up to the free troposphere, smoke plumes from large biomass burning events can reach the upper troposphere and volcanic ash eruptions can transport the ash up to the stratosphere [1]. The main aerosol sources are on the Earth's surface, and aerosol is uplifted under certain weather conditions. Thus, 70% of all aerosol particles are located in the boundary layer [1]. In contrast, dust and smoke are regularly uplifted.

The vertical distribution of aerosol is a key parameter in climate modeling and remote sensing. It is necessary for the calculation of the Earth's energy budget by estimating the direct and indirect radiative forcing of aerosol [2–4]. Aerosol is, in addition to the greenhouse gases, the most important anthropogenic climate forcer. It has both cooling and warming effects. However, uncertainties about aerosol composition and distribution induce uncertainties in the prediction of the climate [5]. Large uncertainties in magnitude and sign of radiative effect originate from unknown or imprecise aerosol layer height (ALH) [3,4]. An example of the impact of aerosol on the Earth's environment is the current warming

of the Atlantic Ocean [6]. We can observe a decrease in Saharan dust emissions and an increase in the temperature of the Atlantic. Saharan dust is transported westward across the Atlantic Ocean. It is assumed that those dust layers in the atmosphere above the ocean had a cooling effect, as light was reflected back to space and not absorbed by the water.

A valid characterization of ALH is also important for the retrieval of numerous parameters from remote sensing data. The uncertainty of CO_2 [7,8] and NO_2 [9] retrieval can be reduced by including the aerosol vertical distribution. Furthermore, aerosol parameter retrievals themselves can be improved with a better knowledge of ALH, e.g., the aerosol retrievals of aerosol optical thickness (AOT) and the single scattering albedo (SSA) from the ultra violet spectral range [10]. In particular, the retrieval of AOT is sensitive to the aerosol height over dark surfaces [11]. Eventually, with a constrained aerosol profile, the atmospheric correction is more accurate, which is important for land and ocean applications, e.g., surface retrievals like the fluorescence [12] or ocean color experiments [13].

The aerosol vertical distribution can be derived on a global scale with remote sensing. Active instruments like the Cloud-Aerosol Lidar with Orthogonal Polarization (CALIOP) mounted on Cloud-Aerosol Lidar and Infrared Pathfinder Satellite Observations (CALIPSO) [14] have a high accuracy of the retrieval of the aerosol height, but due to their small foot print, the global coverage is low [1]. In contrast, passive remote sensing instruments do have good global coverage but often a small sensitivity to aerosol height. However, there have been several sensitivity studies (e.g., [5,15,16]) and attempts to retrieve aerosol height, e.g., from the O_2A absorption band (760–770 nm) or the O_2-O_2 bands (470 nm). As part of a sensitivity study, Colosimo et al. [5] investigated the possibility to retrieve aerosol profiles from O_2 absorption bands with high spectral resolution. They showed that with very high spectral resolution, up to two parameters of the aerosol extinction profile can be retrieved for measurements with a resolution of 0.003 nm. Hollstein and Fischer [16] developed an ALH retrieval for high spectral resolution O_2 measurements with resolutions of 0.3 nm, as it is planned for the Fluorescence Explorer. Dubuisson et al. [17] estimated the uncertainty of an ALH retrieval from MERIS oxygen absorption bands. Preusker and Lindstrot [18] performed a sensitivity study about gaining information about the cloud top pressure from the O_2 absorption from MERIS. They also showed that the retrieval of vertical information from the O_2 band is possible even with low spectral resolution. Spectral high resolution instruments like the Scanning Imaging Absorption Spectrometer for Atmospheric Chartography (SCIMACHY) [15,19], Global Ozone Monitoring Experiment-2 (GOME-2) [20], Orbiting Carbon Observatory 2 (OCO-2) [21] and Tropospheric Monitoring Instrument (TROPOMI) [22] have been used successfully for the retrieval of aerosol height. Also, spectrally coarse top-of-atmosphere (TOA) radiance measurements hold information about the aerosol height as it is shown for ALH retrievals from the Medium Resolution Imaging Spectrometer (MERIS) and PoLarization and Directionality of the Earth's Reflectances (POLDER) [17]. Expected in 2024, the Ocean Colour Instrument (OCI) will be launched on the National Aeronautics and Space Administration's (NASA's) Plankton, Aerosol, Cloud, Ocean Ecosystem (PACE) spacecraft combining the settings of its precursors Visible Infrared Imaging Radiometer Suite (VIIRS) and ozone monitoring instrument (OMI). OCI will have hyperspectral bands within the oxygen absorption bands (O_2A, O_2B (680 nm)) and within the ultra violet band with a spectral resolution of 5 nm and a spectral sampling of 2.5 nm [23]. With this band combination, the OCI shall retrieve the aerosol height for aerosol layers with an AOT larger than 0.1 with an uncertainty of 0.15 km over dark surfaces [24]. The retrieval will be based on the differential optical absorption spectroscopy ratio (DOAS) using an absorbing and a non-absorbing band. A similar method is the spectral fitting method of O_2A and/or O_2B bands as it is applied on measurements of the Earth Polychromatic Imaging Camera (EPIC) sensor on the Deep Space Climate Observatory (DSCOVR) satellite [25]. The aerosol height retrieval of TROPOMI is also based on spectral fitting but with radiance simulations performed by a neural network algorithm [22]. The third common method is the use of the O_2-O_2 band at 477 nm as presented by Chimot et al. [26].

The existing passive remote sensing retrievals of the aerosol height have a rather coarse horizontal spatial resolution but a high spectral resolution (e.g., SCIAMACHY: 0.48 nm, GOME-2: 0.48 nm, TROPOMI: 0.55 nm). The Ocean and Land Colour Imager (OLCI) on Sentinel-3 satellites has a spatial resolution of about 300 × 300 m [27]. OLCI has three spectral bands within the oxygen absorption band with spectral resolution of 2.5–3.75 nm [27]. So far, those bands have not been used to derive the aerosol height. The Sentinel-3 series can be used to collect climate data over a long temporal range [27]. The large fleet of Sentinel-3 (currently Sentinel-3A and Sentinel-3B) allows a global coverage of 2 to 3 days even without including sun glint pixels. As mentioned above, especially for trace gas-retrievals and ocean color algorithms, the aerosol height is an important parameter. By retrieving ALH directly with OLCI, the information could be used to enhance its atmospheric correction and to provide new insight in aerosol–cloud interactions on a small spatial scale. With an ALH product from OLCI, no ALH products from other instruments are necessary, and thus, a spatial overlap of those instruments does not need to be considered.

We use OLCI's radiance measurements in the O_2 absorption band to distinguish low, medium and high aerosol over oceans. We show a sensitivity study on the retrieval of ALH from OLCI O_2A bands, a proof of concept for retrieving ALH over oceans and an uncertainty estimate for the ALH retrieved from OLCI. Due to the steep and distinct oxygen absorption lines, an exact spectral characterization of the O_2A bands is necessary. For the best possible characterization, we use the temporal evolution model of the spectral characterization of OLCI. With this characterization, we can show that OLCI's radiance measurements are sensitive to aerosol height. This is also shown in the application of an aerosol height retrieval on two case studies. For this study, the retrieval is limited to dust and smoke particles in cloud-free scenes over the ocean. It is based on radiative transfer simulations. The radiative transfer model, input data and the retrieval algorithm are described in the Methods Section 2. The results of the sensitivity study and the application of the retrieval on the test scenes are presented in Section 3. The uncertainty of the retrieval is presented in Section 4. The results are discussed in Section 5.

2. Methods

2.1. Radiative Transfer Model

Sensitivity studies and the look-up tables (LUTs) applied in the retrieval of ALH are based on radiative transfer simulations calculated with the vector radiative transfer model, the "matrix operator model" (MOMO), developed at the Freie Universität Berlin [28,29]. The interaction of the light that travels through the atmosphere is described with the radiative transfer equation. Its matrix form is discretized, Fourier-decomposed, and solved by a doubling and adding method [28]. The output of MOMO is the diffuse upward and downward-directed radiance for discrete angles for each atmospheric layer.

The atmosphere is approximated with a model of plane parallel layers with homogeneously distributed particles. The ocean surface is approximated as randomly distributed planes with Fresnel properties. The distribution of the surface normals depends on the wind speed. This dependency is described by Cox and Munk [30]. The ocean interface is described with a refractive index of 1.335 (water temperature: 20 °C; salinity: 36 PSU) with no further description of the water constituents as the studied bands are not influenced by them.

The gas absorption is described by a line-by-line model which is approximated with a k-binning solution [31]. The input of the line-by-line model is taken from the HITRAN16 data base [32]. The oxygen cross sections originate from Drouin et al. [33].

2.2. Setup of Radiative Transfer Simulations

We study the sensitivity of the O_2A absorption bands of OLCI with main focus on the aerosol height. However, the bands are also sensitive to AOT, aerosol type, the surface

roughness, viewing geometry and band characterization. To quantify the sensitivities, we simulate TOA radiances for various quantities of those parameters.

The basic setup describing the ocean and the atmosphere is kept constant. The atmosphere is split in 27 layers. The lower 6 km is split into layers every 25 hPa. We chose the standard Air Force Geophysical Laboratory (AFGL) Atmospheric Constituent Profile [34] for the mid-latitude summer case with a surface pressure of 1025 hPa.

To reduce the number of simulations, the TOA radiance is calculated for four rectangular spectral response functions at 754 nm with a width of 23.5 nm; at 762 nm with a width of 10.4 nm; at 765 nm with a width of 12.9 nm; and at 768 nm with a width of 10.2 nm. From those simulations, we create look-up tables by convolving the simulations with OLCI's spectral instrument response functions.

The ocean roughness is tuned for wind speeds between 3 and 9 m/s. All simulations are made for different observation and sun angles covering the whole hemisphere. The aerosol is placed in one of the following layers with borders at: 1000 hPa (215 m) and 975 hPa (440 m); 950 hPa (665 m) and 925 hPa (890 m); 900 hPa (1117 m) and 875 hPa (1367 m); 725 hPa (2934 m) and 700 hPa (3219 m); 550 hPa (5157 m) and 525 hPa (5530 m). In all other layers but the one where the aerosol is placed, we assume that no aerosol is present. We define the aerosol layer height (ALH) as

$$ALH = \frac{a+b}{2} \tag{1}$$

with a as the lower layer boundary and b as the upper layer boundary. The ALHs of the 5 cases are 327, 777, 1244, 3076 and 5255 m (see Figure 1).

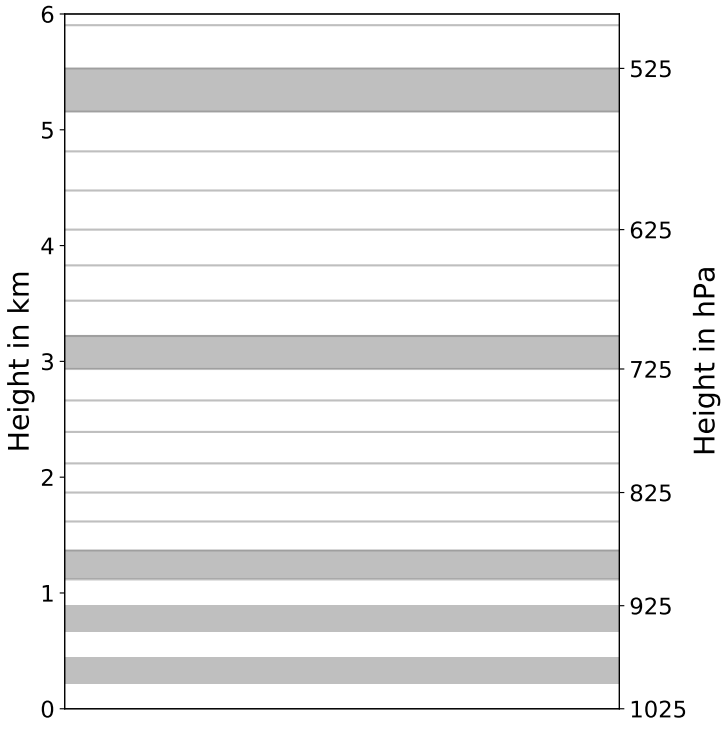

Figure 1. Schematic overview of aerosol vertical distributions for five cases with ALH at 327, 777, 1244, 3076 and 5255 m. The lines indicate the layer interfaces.

We chose two different aerosol models, namely *dust* and *strong absorbing fine mode aerosol* (SABS), which are described in the next section (Section 2.3). AOT at 550 nm ranges from 0.05 up to 12 for dust and up to 5.5 for SABS.

2.3. Aerosol Model

Elevated aerosol particles originate mostly from uplifted desert dust or smoke from biomass burning. We use models that describe those two aerosol types. The spheroid model of Dubovik et al. [35] is used to parameterize dust particles. The model is based on LUTs with simulated size-dependent and shape-dependent optical properties for random oriented particles. The complex shape of dust particles is approximated by spheroids. The microphysical properties were chosen following the hybrid end-to-end aerosol classification model for EarthCARE (HETEAC) [36]. For Saharan desert dust, the refractive index at 550 nm is chosen to be $1.53 + i0.003$, the effective radius is 1.94 µm, the mode radius of the volume size distribution 2.32 µm and logarithmic mode width of 0.6.

Biomass burning aerosol is approximated by strong absorbing spherical fine-mode particles following HETEAC and the Aerosol-CCI approach [36]. This approximation is true especially for fresh smoke particles which have a large fraction of strong absorbing soot and other absorbing material. We chose a particle distribution with an effective radius of 0.14 µm and a spectrally constant refractive index of $1.5 - 0.043i$.

The phase functions are shown in Figure 2 for different scattering angles and depend on the sun zenith angle (SZA) ϕ_{SZA}, the viewing zenith angle (VZA) ϕ_{VZA} and the azimuth difference angle (AZI) θ_{AZI}. It is calculated with the following formula (adapted from [37]):

$$cos(\Theta_{scat}) = sin(\phi_{SZA}) \cdot sin(\phi_{VZA}) \cdot cos(\theta_{AZI}) - cos(\phi_{SZA}) \cdot cos(\phi_{VZA}) \quad (2)$$

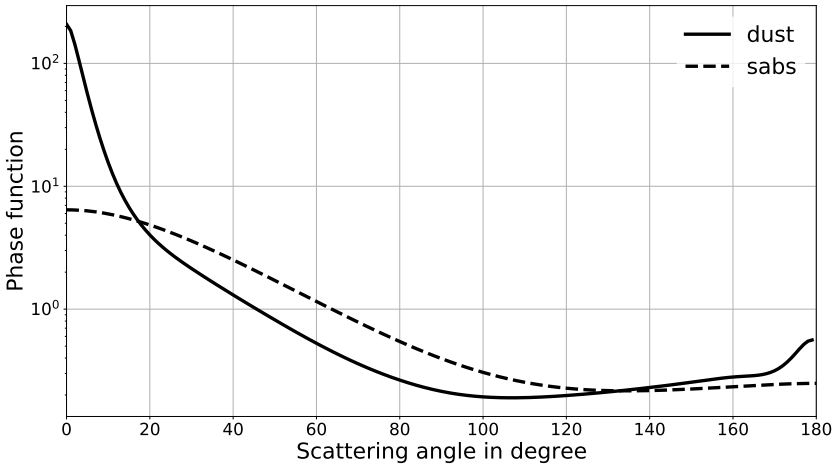

Figure 2. Phase function of aerosol models *dust* in solid lines and *strong absorbing aerosol* (SABS) in dashed lines at 760 nm.

The phase function for the spherical SABS particles is calculated with a Mie scattering algorithm [38]. Further optical properties are shown for dust and SABS in Table A1.

2.4. OLCI Data

OLCI has three bands within the O_2A absorption band, namely Oa13, Oa14 and Oa15, with nominal central wavelengths of 761.25 nm, 764.375 nm and 767.5 nm and nominal full width at half maximum (FWHM) of 2.5 nm, 3.75 nm and 2.5 nm. As a reference band without absorption, we chose the Oa12 band at 753.75 nm with nominal FWHM of 7.5 nm. The relative response functions of those four bands are shown together with the TOA transmission by oxygen in Figure 3. The input of the retrieval is the Level 1 (L1) data, including the radiances at the named bands, the solar flux, the wind speed and the observation and sun geometry. From the given sun and observation azimuth angle, we calculate an azimuth difference angle with 0° pointing towards the sun, marking the sun glint area, and 180° in the backscattering direction.

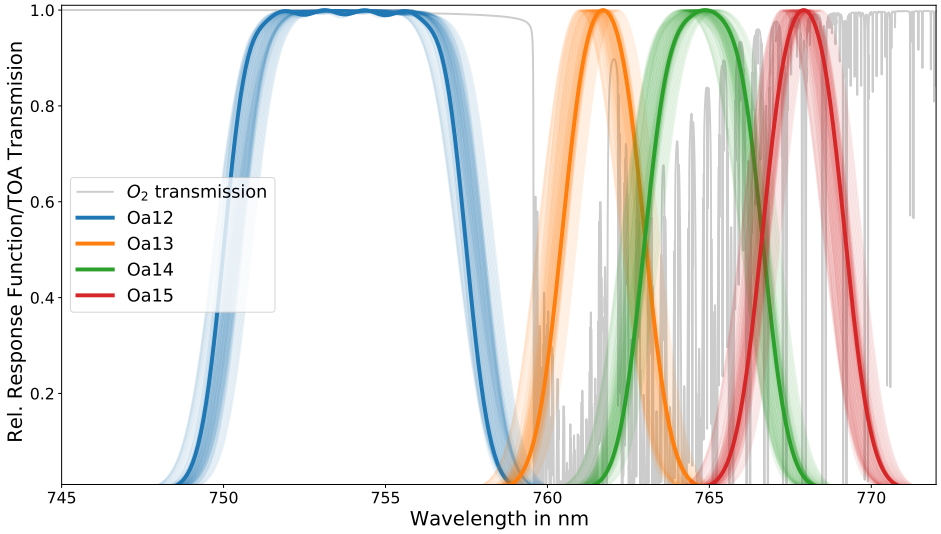

Figure 3. Relative spectral response functions (RSR) of OLCI-B in O_2 absorption band. Transparent colors show RSR of different detectors and non-transparent colors are the harmonized response functions. In grey, the TOA transmission is given for an air mass factor of Section 2.2.

2.4.1. Preprocessing

OLCI is built from 5 cameras with 740 across track pixels each. Each of those pixels has its own spectral response function (see Figure 3). In particular, for the absorption bands, it is crucial to know them as accurately as possible. Due to the deep O_2 absorption lines, only small shifts in the central wavelength result in large differences in the TOA radiance [18]. For the accurate choice of spectral response function, we use the model that characterizes the time evolution of OLCI's spectral responses (see [39] https://sentinels.copernicus.eu/documents/247904/2700436/LUT.zip, accessed on 24 February 2023). Based on this band characterization and on the Sentinel Application Platform (SNAP) plugin for the O2 harmonization of OLCI [40], the data are harmonized to the nominal spectral response function for each band (Oa13, Oa14, Oa15). The harmonization is based on precalculated LUTs of transmissions [41]. First, the OLCI bands 12–16 are normalized with respect to their corresponding in-band solar irradiance. Secondly, reference window radiances are calculated by a spectral interpolation of the window band Oa12 and Oa16 to the nominal spectral position of the bands Oa13, Oa14 and Oa15. With these interpolated reference window radiances, apparent transmissions are calculated for those bands. The apparent transmission is shifted to the nominal wavelength using a combination of KD-search and an inverse distance weighted interpolation [41]. The harmonization method is described in more details in Appendix B.

The harmonized transmissions have the same spectral response function across track, and thus, the LUTs for the ALH retrieval do not need to account for the central wavelength or FWHM. For the sensitivity study, we introduce the central wavelength as dimension of the LUT. The output of the simulations is convolved with the time-evolved spectral response function, which is shown as non-transparent colored lines in Figure 3. For the sensitivity study LUT, the response functions are shifted plus and minus 0.1 nm. In addition to the transmissions at the absorption bands, the radiance of the absorption-free band is used for the retrieval and the sensitivity study.

In Figure 4, the transmission for the band ratio at 761.25 and 753.75 nm is shown before and after the harmonization of the central wavelength. Before the harmonization, the interface between the cameras is clearly visible. The mean difference between camera 3 and 4 along the track is on average 6% with occasional 10% peaks. The harmonized transmission shows only slight camera effects, especially between camera 3 and 4. Here, the peak differences could be eliminated and the mean difference is reduced by 1.5%.

The residual difference is set as measurement uncertainty for the band at 761.25 nm (see Section 2.6).

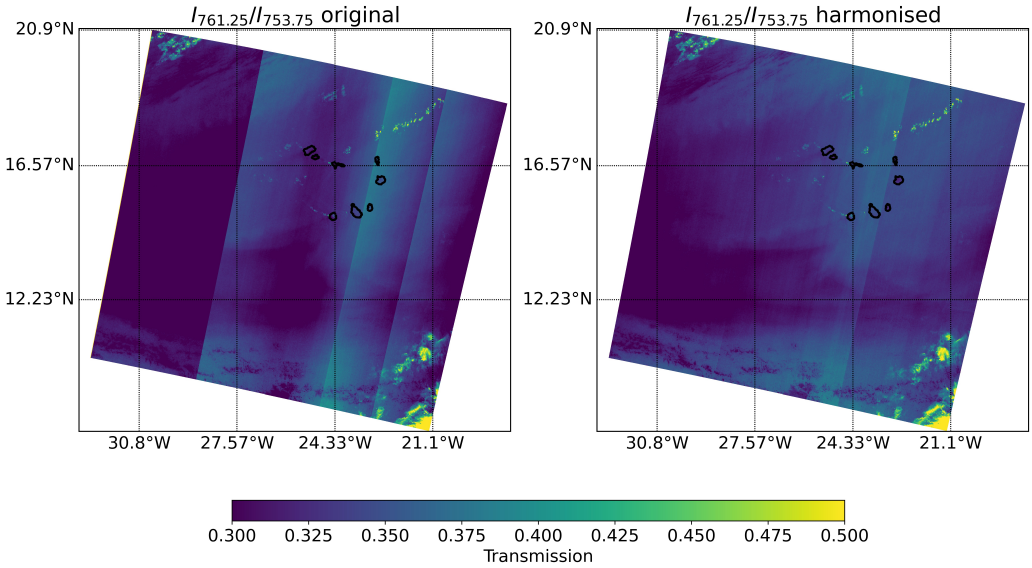

Figure 4. Comparison of original transmission on the **left**, calculated as ratio of OLCI-B L1 radiance at 761.25 and 753.75 nm, and harmonized transmission on the **right**.

2.4.2. Case Study and Reference Data

The retrieval algorithm is applied for two case study scenes: (i) during the large dust storm in summer 2020 called "Godzilla" (see e.g., [42]) and (ii) during a large wild fire at the coast of California in September 2020. Both scenes were selected to match our assumed surface pressure of 1025 hPa.

For the dust scene, we chose two sequences of Sentinel-3B on 18 June 2020 over Cape Verde at 11:35 UTC and 11:38 UTC. The scene is dominated by a large dust plume with a large range of different optical thicknesses and only very few clouds. The two sequences have a mean surface pressure according to the L1 OLCI data of 1015 and 1021 hPa.

For the smoke scene, we chose sequences of Sentinel-3A and Sentinel-3B on 8 September 2020 taken between 18:25 and 18:30 UTC. In the center of the scene is a very thick smoke plume with clouds in the northeast and southwest. The sequences have a mean surface pressure according to the L1 OLCI data of 1011, 1024 and 1025 hPa.

As reference data set, we use the ALH product (S5P_L2__AER_LH version 1 product (https://doi.org/10.5270/S5P-j7aj4gr, accessed on 28 March 2023)) from TROPOMI on board of Sentinel-5P (S5P) from the overpasses on the same days about two to four hours after the Sentinel overpass: on 18 June 2020 at 14:13, 14:18 and 15:53 UTC and on 08/09/2020 between 20:24 and 20:29 UTC. TROPOMI has a spectral resolution within the O_2A band of 0.38 nm with a spectral sampling interval of 0.12 nm and a spatial resolution of 7 km $\times$ 3.5 km [43]. The retrieval is based on a neutral network approach [22].

Furthermore, we compare our results with CALIOP measurements on board of CALIPSO. The active instrument provides the extinction profile at 532 nm with a vertical resolution of 60 m and a horizontal resolution of 5 km. The effective aerosol height can be approximated from the extinction profile by the weighted extinction or the cumulative extinction. Both definitions have been used for the comparison with passive remote sensing [2,44,45]. We use the weighted extinction, which is defined as

$$ALH_{Cali} = \frac{\sum_{i=1}^{n} \beta_{ext,i} * Z_i}{\sum_{i=1}^{n} \beta_{ext,i}}, \quad (3)$$

with $\beta_{ext,i}$ as the aerosol extinction (km^{-1}) at 532 nm at altitude Z_i in km and n number lidar product layers.

We calculate the weighted extinction from the level 2 Aerosol Profile product (https://doi.org/10.5067/CALIOP/CALIPSO/CAL_LID_L2_05kmAPro-Standard-V4-21, accessed on 9 March 2023). For the dust case, we chose the overpass from 18 June 2020 between 03:22 and 03:45 in the morning, which was about eight hours earlier than the Sentinel overpass. For the smoke case, we chose the overpass from 8 September 2020 between 21:45 and 22:07 UTC, which was about three hours after the Sentinel overpass.

2.5. 1D Variational Approach

The retrieval of ALH is based on a 1D variational approach (1Dvar). For given surface and atmosphere description and measurement geometry, ALH and AOT are optimized in order to reduce the difference between measured L1 radiances and forward-modeled radiances. Forward-modeled radiances are calculated by interpolating within the above described LUTs. Following the direction of the largest gradient, ALH and AOT are changed step-wise in an iterative process taking an a priori knowledge, with its uncertainty and the measurement uncertainty into account. The following description of the 1Dvar method and all formulas are adapted from Rodgers [46].

The state vector is one input of the forward model. It includes ALH and AOT in our case. Further, fixed parameters $\boldsymbol{P_a}$, namely the wind speed and the measurement geometry, are the input of the forward model. The state vector $\boldsymbol{X_i}$ is adjusted in each step i using the Gauss–Newton method considering the gradient in terms of the Jacobian $\mathbf{K_i}$ and the measurement error covariance $\mathbf{S_e}$:

$$\begin{aligned} \boldsymbol{X_{i+1}} = \boldsymbol{X_i} - (\mathbf{S_a}^{-1} + \mathbf{K_i}^T \mathbf{S_e}^{-1} \mathbf{K_i})^{-1} (\mathbf{K_i}^T \mathbf{S_e}^{-1} \cdot (\boldsymbol{F}(\boldsymbol{X_i}, \boldsymbol{P_a}) - \boldsymbol{Y}) \\ - \mathbf{S_a}^{-1} \cdot (\boldsymbol{X_a} - \boldsymbol{X_i})) \end{aligned} \tag{4}$$

The difference between forward model $\boldsymbol{F}(\boldsymbol{X_i}, \boldsymbol{P_a})$ and measurement $\boldsymbol{Y}$ is weighted with the measurement error covariance matrix and the Jacobian. Furthermore, the difference between state vector and a priori knowledge $\mathbf{X_a}$ weighted by the a priori error covariance matrix $\mathbf{S_a}$ is taken into account. Once the maximum number of iterations (10) is reached or the increment weighted by retrieval error covariance matrix $\hat{\mathbf{S}}$ is small, the iteration stops. The second stop criterion is given by

$$(\boldsymbol{X_i} - \boldsymbol{X_{i+1}})^T \cdot \hat{\mathbf{S}}_\mathbf{i}^{-1} \cdot (\boldsymbol{X_i} - \boldsymbol{X_{i+1}}) < n \cdot \epsilon \tag{5}$$

with $\epsilon = 0.01$ and $n = 2$ is the number of parameter state dimensions and the retrieval error covariance matrix:

$$\hat{\mathbf{S}}_\mathbf{i} = (\mathbf{S_a}^{-1} + \mathbf{K_i}^T \mathbf{S_e}^{-1} \mathbf{K_i})^{-1}. \tag{6}$$

This method assumes Gaussian probability density functions of uncertainty and bias-free measurements, priors and models.

2.6. Retrieval of ALH from OLCI Level 1 Data

We retrieve the ALH and AOT for cloud-free cases over ocean and for known aerosol types. The input of the retrieval are harmonized, normalized radiance I of the absorption-free band at 753.75 nm and of the absorption bands at i = 761.25, 764.375 and 767.5 nm on a logarithmic scale:

$$Y_i = log(\frac{I_i}{I_{753.75}}). \tag{7}$$

The radiances at the different bands are normalized with their corresponding solar irradiances.

The measurement errors are approximated with a signal-to-noise ratio of 200 for the absorption-free band and of 50 for all other bands. At band i = 764.375 nm and i = 767.5 nm, the Gaussian error propagation gives

$$Y_{erri} = \frac{1}{200} + \frac{1}{50}. \quad (8)$$

To include residual camera effects which are strongest for the band at 761.25 nm (see Figure 4), the mean difference between the last detector row of camera 3 and the first detector row of camera 4 is taken as measurement error for this band.

All four bands are optimized simultaneously. The a priori input for ALH and AOT is chosen for each scene (dust: ALH = 3000 m; AOT = 3.7, smoke: ALH = 1000 m; AOT = 5.5) according to other satellite, ground-based and model data. We use AERONET data for the AOT at 550 nm from Cape Verde for the dust scene, which lies in the center of the large dust plume, and from the AERONET stations at the west coast for the smoke scene which measured AOTs between 5 and 6. The dust ALH is approximated roughly using the back trajectory model Hysplit [47] and using the average of the CALIOP data which were recorded about 12 h earlier than the OLCI data. The smoke ALH is approximated roughly using the cloud top height of MODIS [48]. The choice of a priori parameter is restricted to these case studies. A more general assumption could be based on, e.g., Copernicus Atmosphere Monitoring Service (CAMS) data [49]. The a priori error covariance of ALH is kept very large to ensure a free choice of ALH. In contrast, we chose a small AOT a priori error covariance for robust convergence. The fixed input parameters are the wind speed, SZA, VZA and AZI which are taken from OLCI level 1 data. All inputs for the retrieval are listed in Table 1. The surface pressure, central wavelength and the FWHM are also fixed. They are 1025 hPa and the nominal central wavelengths and FWHMs.

Table 1. Input for retrieval of ALH for the dust and smoke test scenes.

Parameter	Values	Data Source
$\mathbf{Y}$	$(I_{753.75}, log(\frac{I_{761.25}}{I_{753.75}}), log(\frac{I_{764.375}}{I_{753.75}}), log(\frac{I_{767.5}}{I_{753.75}}))$	OLCI L1
$\boldsymbol{S_e[i,i]}$	$(\frac{I_{753.75}}{200})^2, (log(T_{Cam4}) - log(T_{Cam3}))^2, (\frac{1}{200})^2 + (\frac{1}{50})^2, (\frac{1}{200})^2 + (\frac{1}{50})^2$	OLCI L1
$\boldsymbol{P_a}$	wind speed, SZA, VZA, AZI	OLCI L1
$\boldsymbol{X_{a0,0}}$ (AOT)	Dust case: 3.7; Smoke case: 5.5	first guess
$\boldsymbol{X_{a1,1}}$ (ALH)	Dust case: 3000 m; Smoke case: 1000 m	first guess
$\boldsymbol{S_{a0,0}}$ (AOT)	Dust case: $(0.1)^2$; Smoke case: $(0.1)^2$	guess
$\boldsymbol{S_{a1,1}}$ (ALH)	Dust case: $(5000\ \text{m})^2$; Smoke case: $(5000\ \text{m})^2$	guess

3. Results

3.1. Sensitivity Study

The TOA radiance between 760 and 770 nm is mainly determined by the strong absorption features of oxygen. It scales with the surface pressure. However, the surface pressure is a well-known parameter. Consequently, we do not include it in our sensitivity study. Instead, the sensitivity to ALH is studied. The sensitivity study is designed for the OLCI nominal bands Oa12–Oa15 with their central wavelengths at 753.75, 761.25, 764.375 and 767.5 nm and typical observation and sun geometries with SZA of 30°, VZA at 46° and AZI at 170°. In addition to the surface pressure and the measurement geometry, the surface reflectance, aerosol properties and the characterization of the instrument determine the TOA radiance at those bands. Hence, we study the sensitivity of the TOA radiance with respect to the wind speed, which parameterizes the roughness of the ocean surface and thus the surface reflectance over the ocean, ALH, AOT, aerosol type, and the central wavelength

of the instrument bands. The sensitivity is given as derivative with respect to each of the parameters and each band. To reduce the influence of AOT on the TOA signal, we take the ratio of the absorption bands and the absorption-free band at 753.75 nm. The sensitivity study is performed for different aerosol cases with two different aerosol types, namely dust and SABS, with different AOTs (0.15, 0.55, 1) and different ALHs (1100, 3000 and 4900 m).

Results of the sensitivity study for a glint-free scene are summarized in Figure 5. The Jacobians are given in percent. The sensitivity to ALH is given in Figure 5a. The absorption-free band is not sensitive to the aerosol height. The band ratio at 761.25 nm shows the largest sensitivity with a change of more than 8% for thick and low dust layers. The sensitivity increases with AOT and decreases with ALH. The more aerosol particles are present in the atmosphere, the more the signal is changed due to scattering and absorption by the aerosol. In lower layers, the pressure is higher and the number of oxygen molecules is larger. Thus, an aerosol layer closer to the ground has a stronger effect on the TOA signal. Additionally, we observe that the ALH of dust is more sensitive, which can be explained by its optical properties (see Table A1). Dust is scattering more than smoke and thus, more light is reflected to TOA, reducing the interaction of the light with O_2.

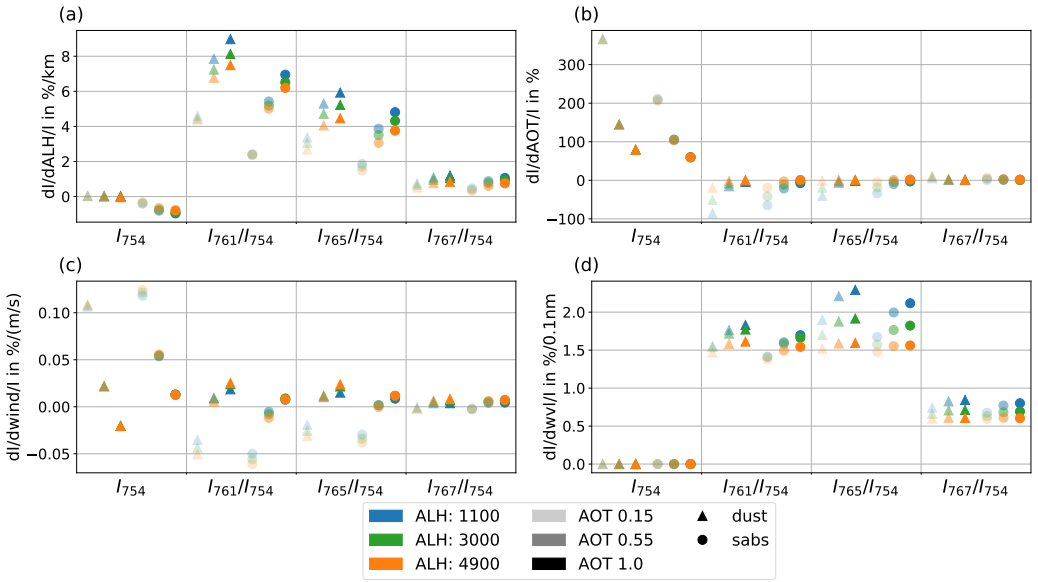

Figure 5. Jacobians of TOA radiance ratios at different central wavelengths relative to (**a**) ALH, (**b**) AOT, (**c**) wind speed and (**d**) central wavelength. Jacobians are given for two aerosol models (circles: SABS, triangles: dust) and for different AOTs (transparent: 0.15, non-transparent: 1.0). All results are given for SZA of 30°, VZA at 46° and AZI at 170°.

The largest sensitivity of the absorption-free signal can be observed for the AOT (Figure 5b). For small AOTs, the signal is changed by 200–380% for changes of 1 in the AOT in the absorption-free band. This strong dependence is true for both aerosol cases. The sensitivity is smaller with 80% for smoke and 60% for dust at AOT of 1. The influence of AOT on the absorption bands is reduced by taking the ratio of absorption band and absorption-free band. For the ratios, the sensitivity to the AOT is small with a maximum at 761.25 nm for small AOTs. The optical depth of dust influences the band ratio with up to 100% at small AOTs of 0.15. For larger optical thickness, the sensitivity to the AOT is reduced to less than 10% for a change in AOT of 1 at 761.25 nm. The band ratios at 764.375 and at 767.5 nm are less sensitive for all AOTs.

The wind speed does not influence the TOA signal strongly for our study case of an off-glint case. Its sensitivity is negligible (see Figure 5c). For a glint observation geometry, the sensitivity is larger than for the off-glint case (see Figure A1). In the absorption-free band the sensitivity can be as high as 3%, which is small compared to the sensitivity to AOT. For the glint case, the sensitivity to the ALH and the central wavelength are very similar

compared to the off-glint case, and the sensitivity to AOT is reduced within the absorption-free bands. However, AOT can only be determined accurately for glint geometry with an exact description of the glint. If we assume a measurement uncertainty of about 0.5% for OLCI and sensitivities to the ALH between 1 and 8%, it is possible to retrieve the ALH from OLCI measurements both in off-glint and glint geometries. Only aerosol layers with small AOTs are difficult to retrieve.

Another sensitivity parameter is the central wavelength (see Figure 5d). Again, the sensitivity is only high in the absorption bands, which is due to their steep and distinct nature. A change of the central wavelength of 0.1 nm changes the TOA signal between 1.5 and 2% for both aerosol types. The sensitivity to the wavelength is larger than the uncertainty of the measurement and thus it will be relevant in the retrieval. We use the temporal evolution model for the instrument characterization, which has an uncertainty of 0.1 nm. Hence, the accuracy of the definition of the central wavelength limits the retrieval accuracy. The wavelength uncertainty of 0.1 nm contributes to the uncertainty budget of the ALH by approximately 200 m in band Oa13, 500 m in band Oa14, and 1000 m in band Oa15. The uncertainty of the retrieval using all three bands simultaneously is further discussed in Section 4.

Using this sensitivity analysis, we showed that it is possible to retrieve ALH from OLCI measurements for dust and smoke with an resolution better than 1 km and with the restriction of a well known instrument characterization with a central wavelength accuracy of 0.1 nm. Additionally, the aerosol type must be known.

3.2. Retrieval of ALH for Test Cases

We apply the retrieval of the ALH to two scenes, one showing elevated dust particles over the Atlantic Ocean west of Africa and one showing smoke particles over the Pacific Ocean from a forest fire on the west coast of North America. For each scene, the LUT is chosen according to the known aerosol type and an a priori is assumed. We consider only pixels with a retrieved AOT larger than 0.55. This threshold is selected based on the sensitivity study and it can be further adjusted. For lower AOTs, the influence of a change in AOT by 0.1 is stronger than a change in ALH by 1 km.

3.2.1. Dust Case

Two sequences of OLCI-B from 18/06/2020 over Cape Verde are evaluated and compared with TROPOMI and CALIOP (see Section 2.4.2). The true color image (RGB) from OLCI-B is shown in Figure 6a. A thick dust cloud is visible with varying AOT. Only small parts of the images are covered by clouds. Clouds are flagged out using the IDEPIX algorithm, which is implemented in SNAP [50]. The red line shows the CALIOP-track (of sub-satellite points) from 03:29 UTC in the upper subfigures. The two OLCI sequences are taken only 3 min apart from each other at 11:35 UTC and 11:38 UTC. Across the track, we cannot observe any camera artefacts.

Figure 6b shows the retrieved ALH in kilometers. Clouds are flagged out, which is indicated by white pixels. The retrieval did not converge for the light grey pixels, and the dark grey pixels are flagged out due to found AOT smaller than 0.55. The main reason for non-convergence is a low aerosol loading as present in the northwest. Comparing our results to the ALH retrieved from TROPOMI measurements (Figure 6c), we can observe the same distribution of ALHs. A higher dust plume is present around 22°N, gradually decreasing southward. The lowest aerosol layers are at 12.6°N, which is true for both ALH retrievals from TROPOMI and OLCI. Higher particles are present at about 10°N. Overall, the OLCI ALH is a bit larger than the one of TROPOMI. The western TROPOMI images were recorded at 15:53 UTC and the eastern images at 14:13 and 14:18 UTC. The images fit together very well, which indicates a stable situation. Additionally, we investigated different CALIPSO overpasses at 03:29 and 15:29 UTC, which both showed a dust plume at the same height at similar latitudes. From these observations, we are confident, that we can compare our results measured between 11:35 and 11:38 UTC both with the TROPOMI

data and the CALIPSO overpass at 03:29 UTC (see Figure 6d). The afternoon overpass of CALIPSO did not cover our study scene.

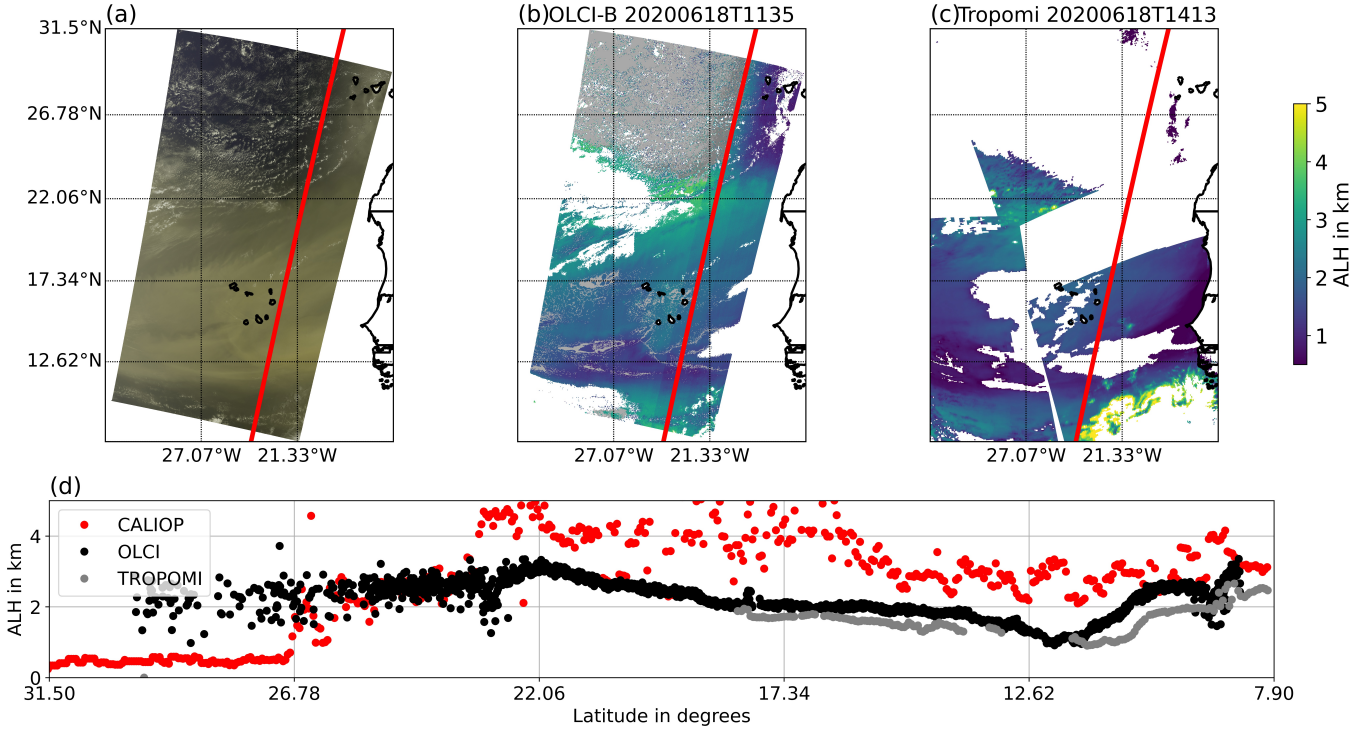

Figure 6. (**a**) RGB composite generated from OLCI L1 on 18/06/2020 between 11:35 and 11:38 UTC over the Atlantic west of central Africa. (**b**) Optimized ALH derived from OLCI-B measurements (**c**) TROPOMI ALH on 18/06/2020 at 14:13, 14:18 and 15:53 UTC. (**d**) CALIOP, OLCI and CALIPSO ALH along CALIPSO track on 18/06/2020 at about 03:29 UTC. White pixels are cloud flags, light grey pixels are non-convergence pixels and dark grey pixels are flagged out due to AOT smaller than 0.55. The red line in a–c shows the same CALIPSO track as in (**d**).

Figure 6d shows the weighted extinction from the CALIPSO overpass at 03:29 UTC and the co-located OLCI-B and TROPOMI ALHs. Along the CALIPSO track at 03:29 UTC, the overall ALH distribution from OLCI and TROPOMI is similar to the weighted extinction from CALIOP with the exception for higher latitudes. Here, only a few aerosol particles are present and the pixels are in the sun glint geometry (see Figure A2), which reduces the sensitivity of our retrieval. The TROPOMI ALH is flagged out in this part of the image. All valid TROPOMI ALH are very similar to the OLCI ALH with a slight negative median offset of about 0.5 km. Considering only latitudes between 8° and 23°N, OLCI's ALH is about 1.25 km lower than the one of CALIOP but closer to the CALIOP data than TROPOMI.

3.2.2. Smoke Case

We evaluate a smoke case using sequences of OLCI-A and OLCI-B from 08/09/2020 and nearest overpasses of CALIPSO and S5P. The true color image generated from OLCI L1 measurements in Figure 7a shows a thick smoke plume over the Pacific Ocean west of California. The western image originates from OLCI-B. The eastern part of the image are two OLCI-A scenes. The red line marks the CALIOP track of sub-satellite points in all three upper subplots.

Figure 7b shows the retrieved ALH from those OLCI sequences. We did not apply the IDEPIX cloud mask as it flagged our target smoke plume. Thus, Figure 7b does not show white marked pixels. The ALH retrieval flagged out the cloud pixels, e.g., in the northwest, anyway, as those pixels did not converge (see light grey pixels in Figure 7b). In

addition to cloudy pixels, the retrieval also failed for parts of the smoke plume. Here, the L1 radiance was very bright which is not represented in our SABS LUT. However, the height of the eastern parts of the thick smoke plume (at longitudes between 124° and 130°W and latitudes between 45.5° and 41.5°N) could be estimated. The plume is low compared to the thinner plumes in the north (at longitudes between 124.5° and 132°W and latitudes between 47.5° and 46.5°N). In contrast, in the very south of the scene, the smoke plume is estimated at a high altitude of up to 5 km.

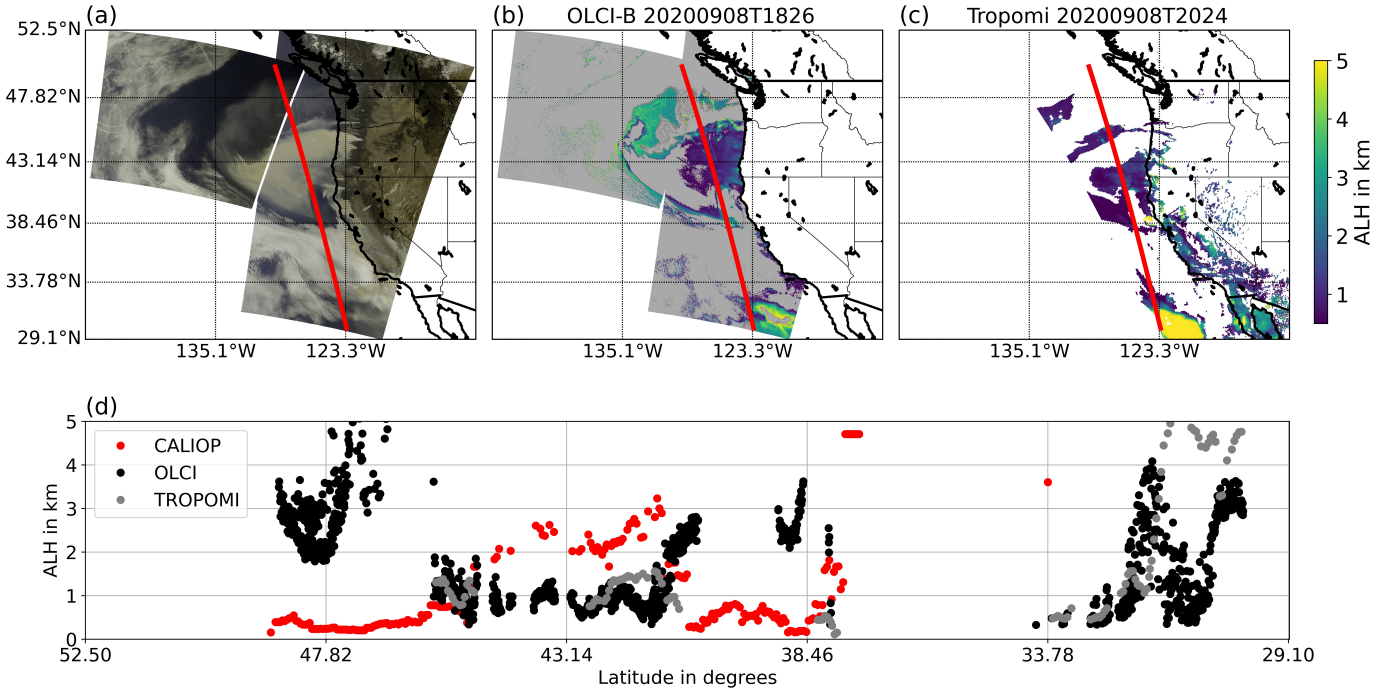

Figure 7. (**a**) RGB composite generated from OLCI L1 on 8 September 2020 at 18:26 UTC in west of California. (**b**) Optimized ALH derived from OLCI-B measurements. (**c**) TROPOMI ALH on 8 September 2020 at 20:24 and 20:29 UTC. (**d**) OLCI, CALIPSO and TROPOMI ALH along CALIPSO track on 08/09/2020 at 21:27 UTC. The red line in (**a**–**c**) shows the same CALIPSO track as in (**d**).

Comparing to TROPOMI's ALH given in Figure 7c, we can observe similar features in the ALH with high ALH in the south (at longitudes of around 123°W) and low ALH in the main plume (at longitudes between 124° and 130°W and latitudes between 45.5° and 41.5°N). Similar to our retrieval, TROPOMI flags out parts of the main plume (white pixels). Only in the northwest (at longitudes between 134° and 130°W and latitudes between 47.8° and 45.5°N), our results deviate from TROPOMI's ALH. Our ALH (about 3 km) is higher than the one of TROPOMI (about 1 km). Here, the AOT is lower than in the main plume.

The direct comparison of OLCI, TROPOMI, and CALIOP in Figure 7d also shows a good agreement of OLCI and TROPOMI. In the south, at around 31°N, TROPOMI measures a high aerosol layer, whereas OLCI detects a low ALH. However, this area is very cloudy and the conditions could have changed slightly between 18:26 UTC (OLCI overpass) and 20:24/20:29 UTC (TROPOMI overpass). Both retrieval results show differences compared with the weighted extinction measured by CALIOP. The main smoke plume is observed between 40 and 45°N. Here, OLCI's and TROPOMI's ALH is more than 1 km lower. In the north at around 47.8°N, our estimated ALH is higher than the CALIOP one. The difference in the north could be either explained by difference in measurement time or uncertainties within our retrieval. As TROPOMI also shows lower values in the north than OLCI, the discrepancy might be the result of a high uncertainty due to the small AOT for those pixels.

4. Uncertainty Propagation

We estimate the uncertainty of the retrieved ALH by applying a complete linear uncertainty propagation and using a bootstrap method evaluating simulated radiances with known noise. For both methods, all uncertainty sources must be quantified. For some parameters we could only guess them in all conscience. Nevertheless, by applying both methods we can give a sophisticated guess of the ALH uncertainty.

4.1. Linear Uncertainty Propagation

The linear uncertainty propagation is based on the error covariance matrix calculated with Equation (6). It includes the a priori error covariance, the Jacobians with partial derivatives of the radiance with respect to the ALH and the error covariance matrix $\mathbf{S_e}$, which is substituted by the sum of all known uncertainty sources (adapted from [46]):

$$\mathbf{S_e^*} = \mathbf{S_{e_{param}}} + \mathbf{S_{e_{SNR}}} + \mathbf{S_{e_{wvl}}} \tag{9}$$

$\mathbf{S_{e_{param}}}$ is calculated with parameter error covariance matrix $\mathbf{S_{param}}$, which is in the parameter space. $\mathbf{S_{param}}$ includes the input parameter uncertainties, which are transformed to the measurement space using the derivatives of the TOA signal with respect to the parameters (parameter Jacobian ($\mathbf{K_{param}}$) (adapted from [46]):

$$\mathbf{S_{e_{param}}} = \mathbf{K_{param}}^T \mathbf{S_{param}} \mathbf{K_{param}}. \tag{10}$$

The diagonal elements of $\mathbf{S_{param}}$ are the approximated uncertainties of the wind speed, the SZA, VZA and AZI, which are summarized in Table 2. The angles have a very small uncertainty. Nevertheless, we chose perturbations up to 3° to change the scattering angle slightly and thus change the sampling point of the phase function. The off-diagonal elements of $\mathbf{S_{param}}$ are set to zero because the wind speed and the observation geometry are not correlated.

Table 2. Input for simulated truth and assumed uncertainty for the uncertainty propagation.

Parameter	Input Values	Uncertainty
ALH in m	450, 750, 1000, 3000, 5000	-
AOT	0.55–5.5	-
wind speed in m/s	4, 6, 8	$+/-1$
SZA in Degrees	25–40	$+/-3$
VZA in Degrees	0–60	$+/-3$
AZI in Degrees	10–50; 130–150	$+/-3$
wvl in nm	753.75, 761.25, 764.375 and 767.5	$+/-0.1$

$\mathbf{S_{e_{SNR}}}$ gives the contribution of the measurement uncertainty on the diagonal matrix elements (see Table 1). The off-diagonal elements of $\mathbf{S_{e_{SNR}}}$ are set to zero since correlations are not quantified in the instrument characterization. Hence, this uncertainty source is neglected.

The uncertainty contribution of the wavelength is estimated comparing two sets of forward simulations for which known state parameters of all valid pixels including the retrieved ALH and AOT have been applied. One set of forward simulations uses the correct central wavelength, and one set is based on a spectral response function shifted by 0.1 nm. Both sets of simulations are created for all four bands. The mean squared difference of those two sets gives an estimate of the contribution by the wavelength uncertainty. The elements of the error covariance matrix are calculated by multiplying the square root of mean squared differences of the bands scaled with the correlation coefficient c_{ij}:

$$\mathbf{S_{e_{wvl}}}_{ij} = \sqrt{\frac{\sum(I_i^0 - I_i^{0.1})^2}{N}} * \sqrt{\frac{\sum(I_j^0 - I_j^{0.1})^2}{N}} * c_{ij}. \tag{11}$$

i, j are integers between 0 and 3 counting the dimension of the used bands, and N counts all pixels.

The pixelwise uncertainty is presented in Figure 8 for the dust case study scene and in Figure 9 for the smoke case study scene. Both figures show the retrieved ALH and the corresponding uncertainty for all valid pixels. As described before, cloudy pixels are flagged out with white color, non-converging pixels are shown in light grey, and in dark grey are all pixels with retrieved AOT smaller than 0.55. Pixels with small optical thickness have a large ALH uncertainty. In the northeast in Figure 8 at the border to the flagged out pixels, the uncertainty is about 1000 m. The reason for the high uncertainty in this area is the combination of a low AOT and the sun glint. The dependence of the ALH uncertainty on the AOT is discussed in more details in Figure A4a. A decrease in the uncertainty of the ALH is shown for decreasing AOT, which is more prominent in the sun glint area. The observation geometries and the sun glint risk area according to the L1 flag are shown in Figure A2. In the upper right corner of the image, the uncertainty is low even though it is still in the glint area. However, the thick AOT reduces the sensitivity to the glint for this scene. The same is true for the southern glint area (east of the image). Here, the uncertainty is not higher than in the rest of the scene. The optical thick dust cloud reduces the effect of the glint and the ALH can be retrieved with a good precision. Over all, the uncertainty of the ALH for the dust scene is mostly between 400 and 600 m with no dependency on the ALH. With this precision, we can distinguish between low, medium and high aerosol layers even with OLCI's low spectral resolution.

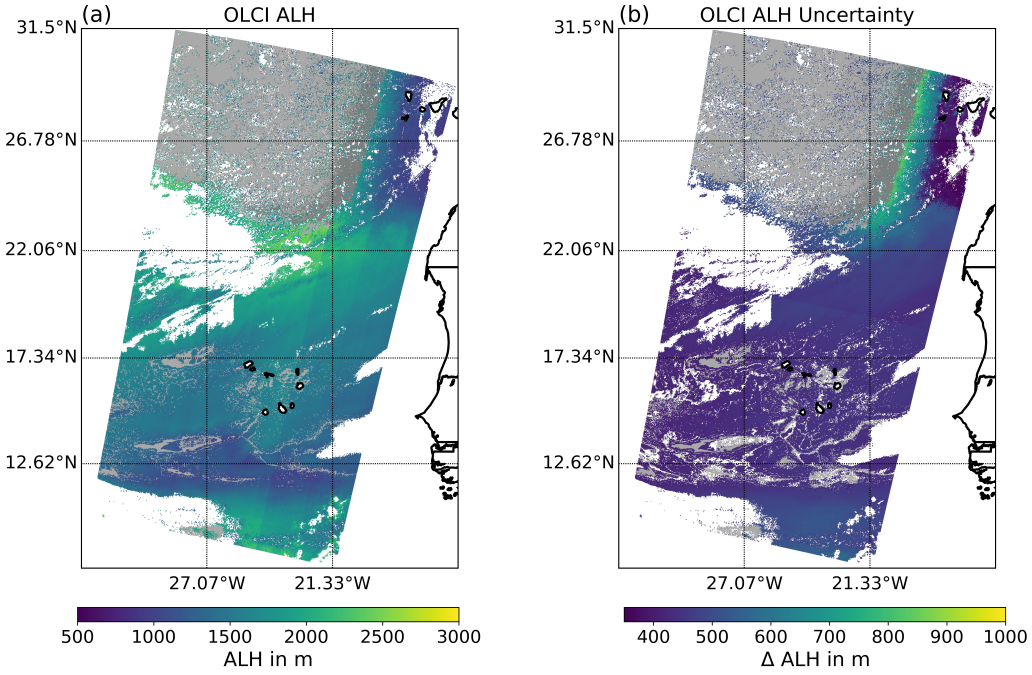

Figure 8. (**a**) Optimized ALH derived from OLCI-B measurements on 18 June 2020 between 11:35 and 11:38 UTC over the Atlantic west of central Africa. (**b**) Estimated pixelwise uncertainty using linear uncertainty propagation. White pixels are cloud flags, light grey pixels are non-convergence pixels and dark grey pixels are flagged out due to AOT smaller than 0.55.

The precision for the smoke case in Figure 9 is even higher. Especially in the area of large AOTs, the uncertainty ranges between 150 and 300 m. Only in the northwest, where the AOT is small, the uncertainty is up to 800 m. At the border between the OLCI-A and OLCI-B image, a jump in the uncertainty can be observed which is not present for the ALH itself. The uncertainty is high for the observations in glint geometry and low for the off-glint geometry. This effect is discussed in the Appendix (see Figure A4b). The jump in uncertainty in our test scene must be differentiated between the northern part, where the

AOT is low in both, S3A and S3B sequence, and the southern part, where the AOT is only low in the S3B sequence. In the northern part, the jump can be explained by the difference in geometry (see Figure A4b). The southern part differs in the AOT strongly and thus the ALH uncertainty decreases from west to east. The glint risk areas are shown in Figure A3.

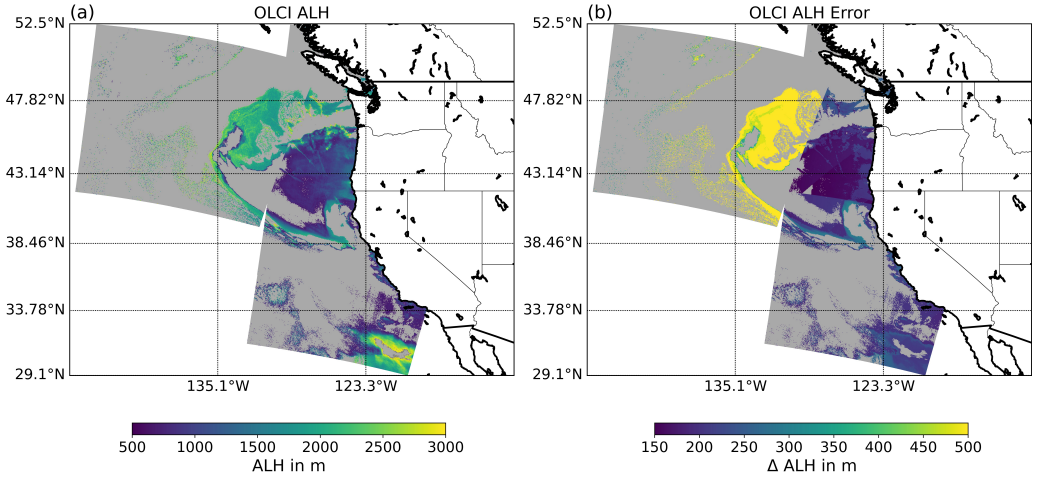

Figure 9. (**a**) Optimized ALH derived from OLCI measurements on 08/09/2020 at 18:26 UTC over the Pacific west of California. (**b**) Estimated pixelwise uncertainty using linear uncertainty propagation. White pixels are cloud flags, and light grey pixels are non-convergence pixels.

4.2. Uncertainty Based on Bootstrap Method

In the bootstrap method, noisy simulated radiances serve as input for the retrieval. The retrieved ALH is compared to the result of the retrieval for the same simulated radiance measurement but without noise. As a first step, about 37,000 cases were simulated to serve as truth. Those cases result from all possible combinations of chosen ALH, AOT, wind speed and measurement geometries. All simulations were performed at the nominal central wavelength and a shifted central wavelength by $+/-$ 0.1 nm. The ranges of the input parameter and the respective noise are given in Table 2. The a priori knowledge for the retrieval is chosen to be 1000 m for the ALH and 3.5 for the AOT in all cases. The a priori and the state error covariances are given in Table 1.

Our bootstrap method comprises 1,000,000 iterations. Each time one of the 37,000 truths were selected randomly. Additionally, the other input parameters were chosen randomly within their uncertainty range (Table 2). The retrieval is done for the perturbed pixels and the truth. The frequency distribution of the difference of both retrieved ALH is given in a histogram in Figure 10. The method is applied for 37,000 dust and 37,000 SABS cases. To study the uncertainty according to the aerosol type, the method is also applied on simulated truth with dust particles which are retrieved using LUTs based on SABS particles and vice versa. The corresponding frequency distributions of differences in the ALH are given in Figure 10b.

The histograms in Figure 10 show only cases in which the retrieval converged. In the case of dust, about 75% of all cases converged, and in the case of SABS, about 65% converged. Most non-converging pixels belong to low AOT cases. The distributions of the difference for retrieved truth with and without noise with the correct aerosol type show a Gaussian-like shape with a small negative bias. The dust case distribution is less wide than the SABS case as the optical properties of dust have a stronger contrast to the signal originating from the ocean surface. The standard deviation is 230 m for dust cases. The standard deviation for SABS cases is 420 m.

The investigation using the wrong aerosol types shows larger differences between perturbed and non-perturbed retrieved ALH. In particular, the retrieval for the dust aerosol layer based on SABS LUTs does not show a Gaussian shape (yellow histogram in Figure 10b). Here, the AOT can not compensate due to the error in the aerosol type. The optical

properties of SABS cause a saturation of the TOA radiance for AOTs larger than 5. Thus, the SABS LUT is limited to smaller radiances. The retrieval based on the dust LUT is more robust with regard to the aerosol type. The distribution is almost Gaussian with a standard deviation of 630 m. With this uncertainty, we can still find appropriate ALH even using the wrong aerosol type. However, the retrieval does not converge as frequently in both cases. Thus, our retrieval method is rather applicable for cases of a known aerosol type.

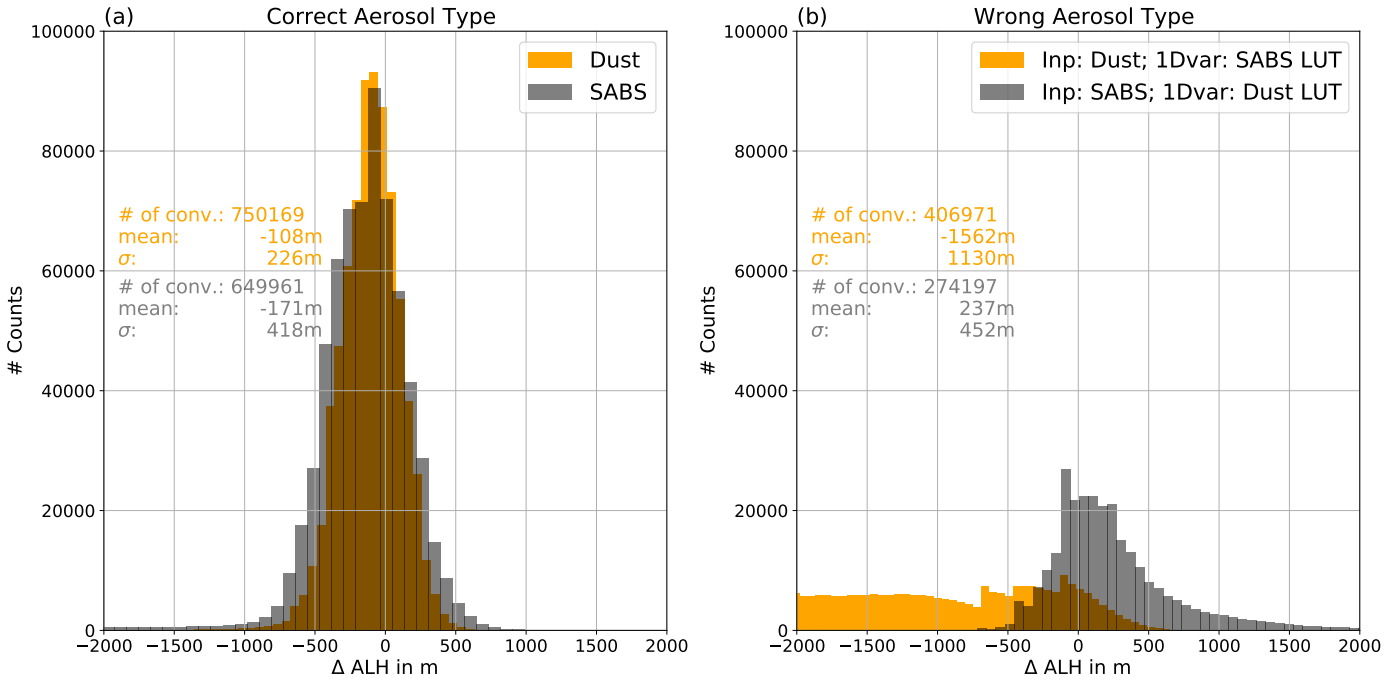

Figure 10. Histograms of differences of all 1,000,000 retrieved ALH with and without noise for dust in yellow and SABS in grey using the LUT (**a**) based on the correct aerosol type and (**b**) based on the wrong aerosol type.

5. Discussion

This study contains a sensitivity analysis for the radiance in OLCI's O_2 absorption bands with respect to ALH, the application of an ALH retrieval to two OLCI test scenes over ocean and an appropriate uncertainty estimation. We found that band ratios of OLCI bands within the O_2A absorption band are sensitive to ALH. A retrieval of ALH is possible for thick dust and smoke plumes if the aerosol type is known and the spectral characterization of the instrument is considered. The sensitivity of the absorption bands to the ALH increase for increasing AOTs. Hence, we chose an AOT of 0.55 as threshold for the application of the ALH retrieval. Pixels with lower AOT are flagged out after the retrieval. This threshold was chosen to minimize the uncertainty of ALH which decreases with AOT. In a MERIS study under similar conditions and a similar accuracy of the spectral characterization by Dubuisson et al. [17], they found a standard error on the retrieval of the altitude of 0.5 km for an AOT of 0.6. Their retrieval was limited on the ALH assuming a known AOT. Dubuisson et al. [17] also showed that for low AOTs, the method is less accurate.

The ALH could be retrieved from OLCI for the dust and the smoke test scene with an uncertainty between 400 and 600 m for a dust scene and with uncertainty as low as 150 m for the smoke scene for off-glint pixels with a low ALH and high AOT. Our generalized uncertainty estimation using the bootstrap method based on simulated measurements resulted in uncertainties of 230 m for dust and 420 m for SABS. Those ALH uncertainties are comparable to the MERIS results shown in Dubuisson et al. [17]. Our uncertainty analysis does not include uncertainties due to the surface pressure, which is a sensitive parameter within the O_2A absorption band. We minimized the uncertainty due to the surface pressure

by selecting a matching surface pressure to the test scenes for the simulation. The retrieval was not successful for pixels with small optical thicknesses or undetected clouds. For converging pixels, we found very similar ALHs for optical thick aerosol layers compared to the TROPOMI ALH. The median difference was about 500 m for the dust case, which lies a bit above our estimated uncertainty range. Comparing OLCI's ALH to the weighted extinction from CALIOP, the weighted extinction is about 1.25 km higher than OLCI's dust ALH. This difference could have several reasons, e.g., the definition of height or the set up of our retrieval using a fixed aerosol model and homogeneous aerosol layer. Nevertheless, our ALH follows the pattern of the one measured by CALIOP. Thus, our aim of distinguishing low, medium and high aerosol layers from OLCI's O_2 absorption bands is achieved. Additionally, OLCI's high spatial resolution allows the observation of very fine spatial structures in the ALH.

The smoke case pixels did not converge as frequently even for large optical thicknesses. Our SABS LUT is limited to relatively small radiances due to the optical properties of SABS. Real-case smoke not only contains SABS but also other particles. For future retrievals, a more complex aerosol model could be used. Converged pixels showed similar ALHs as retrieved from TROPOMI. As for the dust case, those ALHs were lower than the ones measured by CALIOP.

Our retrieved ALH showed systematic differences compared to the height from CALIOP. Similarly, validation studies for TROPOMI's ALH resulted in differences between TROPOMI and CALIOP for thin smoke plumes of about 700 m [51], of 1030 m for different cases [44] and of 510 m for dust and smoke cases over ocean when comparing with a ground-based LIDAR (EARLINET) [52]. Generally, TROPOMI measured lower ALHs than CALIOP, which we also observed in our test scenes. Overall, the differences between OLCI's ALH and CALIOPs ALH are comparable to the ones found for TROPOMI. Chen et al. [53] developed an improved ALH retrieval algorithm for TROPOMI, including also the O_2B band. The improved TROPOMI algorithm is applied to the same test scenes as described in this paper. Using also the O_2B band, the ALH is about 2 km higher in the dust case and about 1 km higher in the smoke case compared to the standard TROPOMI ALH product [53]. Compared to our ALH product, the improved ALH agrees better with the CALIOP observations. However, OLCI does not cover the O_2B absorption band and thus this improvement can currently not be applied for OLCI. The planned advanced OLCI will be hyperspectral, covering both O_2A and O_2B bands. Hence, the future OLCI verison could be even more suitable for ALH retrievals.

Our sensitivity study and retrieval algorithm are limited to two aerosol models, one homogeneous aerosol layer and an underlying ocean surface. We showed that the retrieval works more robustly knowing the aerosol type. However, in operational cases, it is difficult to determine the aerosol type. We showed that the retrieval based on a dust aerosol model converges for some cases without a large increase in the uncertainty. In future, either an aerosol type characterization based on the complete spectral range of OLCI or a synergy product with Sentinel-3 Sea and Land Surface Temperature Radiometer (SLSTR) could be developed to distinguish between dust and smoke aerosol. Another possibility to characterize the aerosol type is to use Copernicus Atmosphere Monitoring Service (CAMs), which delivers information about aerosol [54]. Our retrieval is limited to scenes with large AOTs. It is successful with an uncertainty of a few hundred meters which was demonstrated for two test scenes. Further validations are necessary, e.g., compassion with ground-based measurements. We did not study the effect of different vertical distributions on the uncertainty. In nature, the vertical profile can be very complex with exponential decays or multi-layer profiles. The limited spectral resolution does not provide information about the vertical distribution. Hence, the remaining uncertainty should be estimated. Furthermore, the retrieval could be generalized also for land surfaces. For a retrieval of the ALH over land, the surface must be very well spectrally characterized.

Overall, we could show that it is possible to retrieve the ALH from OLCI measurements, which could allow the determination of ALH for long time series, improvement

of ocean color products, improvement of atmospheric corrections and further studies of aerosol cloud interactions. Even with the limited precision due to OLCI's spectral resolution, the ALH retrieved by OLCI has a high spatial resolution and coverage. Thus, OLCI can deliver useful information about the aerosol vertical distribution.

Author Contributions: Conceptualization, L.K.J. and R.P.; methodology, R.P.; software, L.K.J. and R.P.; validation, L.K.J.; formal analysis, L.K.J.; investigation, L.K.J.; resources, L.K.J.; data curation, L.K.J., R.P. and N.D.; writing—original draft preparation, L.K.J.; writing—review and editing, L.K.J., R.P. and N.D.; visualization, L.K.J.; supervision, J.F. All authors have read and agreed to the published version of the manuscript.

Funding: The studies presented in this paper were conducted alongside the ESA-founded project "Sentinel3 FLEX Tandem Processing Experiment" SF-TAPE. We thank the ESA for the funding. The LUTs for the temporal evolution of the spectral characteristics have been prepared by Rene Preusker as part of the S3MPC under contract to ESA and funded by the EC Copernicus budget.

Data Availability Statement: The OLCI L1 data and TROPOMI ALH data are publicly available at the Copernicus Open Access Hub (https://scihub.copernicus.eu/, accessed on 17 March 2023). The CALIOP data are publicly available, e.g., at https://www.earthdata.nasa.gov/, accessed on 9 March 2023. The temporal evolution model for OLCI's spectral response can be found at https://sentinels.copernicus.eu/documents/247904/2700436/LUT.zip, accessed on 24 February 2023.

Conflicts of Interest: The authors declare no conflict of interest.

Abbreviations

The following abbreviations are used in this manuscript:

ALH	Aerosol Layer Height
CALIOP	Cloud-Aerosol Lidar with Orthogonal Polarization
CALIPSO	Cloud-Aerosol Lidar and Infrared Pathfinder Satellite Observations
SCIMACHY	Scanning Imaging Absorption Spectrometer for Atmospheric Chartography
GOME-2	Global Ozone Monitoring Experiment-2
OCO-2	Orbiting Carbon Observatory 2
TROPOMI	Tropospheric Monitoring Instrument
TOA	Top of Atmosphere
MERIS	Medium-Resolution Imaging Spectrometer
POLDER	PoLarization and Directionality of the Earth's Reflectances
OCI	Ocean Colour Instrument
NASA	National Aeronautics and Space Administration
PACE	Plankton, Aerosol, Cloud, Ocean Ecosystem
VIIRS	Visible Infrared Imaging Radiometer Suite
OMI	Ozone Monitoring Instrument
DOAS	Differential Optical Absorption Spectroscopy
EPIC	Earth Polychromatic Imaging Camera
DSCOVR	Deep Space Climate Observatory
OLCI	Ocean and Land Colour Imager
AFGL	Air Force Geophysical Laboratory
LUT	Look-Up table
MOMO	Matrix Operator Model
AOT	Aerosol Optical Thickness
HETEACT	Hybrid End-To-End Aerosol Classification Model for EarthCARE
SABS	Strong Absorbing Aerosol
SSA	Single Scattering Albedo
SZA	Sun Zenith Angle
VZA	Viewing Zenith Angle
AZI	Azimuth Difference Angle
FWHM	Full Width at Half Maximum
L1	Level 1

S5P	Sentinel-5P
1Dvar	1D Variational Approach
RGB	True color image
IDEPIX	Identification of Pixel
wvl	Wavelength
ESA	European Space Agency
SLSTR	Sea and Land Surface Temperature Radiometer

Appendix A. Aerosol Optical Properties

The optical properties at 755 nm are shown for dust and SABS in Table A1. Comparing dust and SABS, the SSA of dust is almost one, whereas the SSA of SABS is smaller than one. The relative extinction coefficient is given as ratio of the extinction coefficient at 550 nm and 755 nm. The dust relative extinction coefficient larger than one shows its strong scattering properties, whereas SABS absorbs more light than it scatters. The wavelength-dependency of the extinction coefficient is given by the angstrom exponent given for the wavelengths 550 nm and 755 nm. The wavelength dependence of the phase function $p(\Theta)$ is given by the asymmetry factor g [55]:

$$g(\lambda) = \frac{1}{2}\int_{-1}^{1} p(cos\Theta)dcos\Theta \tag{A1}$$

Table A1. Aerosol optical properties at 755 nm for dust and SABS.

Aerosol Property	Dust	Strong Absorbing Aerosol
SSA	0.98	0.76
Rel. Extinction coeff. to 550 nm	1.04	0.56
Angstrom exponent (755/550)	−0.11	1.748
Asymmetry factor g	0.72	0.565

Appendix B. Harmonization Method

The background of the harmonization is a sensitivity factor of the apparent transmission t calculated from the normalized radiances I_i^N measured outside and within the absorption band:

$$t = \frac{I_i^N}{I_{12}^N}(i = 13, 14, 15) \tag{A2}$$

ξ quantifies deviations due to changes of the band central wavelength and bandwidth with respect to their nominal spectral characterization. The foundation is a look-up table that has been calculated from transmissions for nominal band characteristics as well as for all sensible modifications of the band characteristics. The sensitivity factor is the ratio between the transmission with actual band characteristics to the transmission with nominal characteristics.

$$\xi = \frac{t(\lambda, FWHM)}{t_{nominal}} \tag{A3}$$

The sensitivity factor has been calculated for a multitude of photon paths through an atmosphere, reflecting cases without clouds, with thin, thick, high and low clouds above dark and bright surfaces. The gas absorption is based on HITRAN16 [32]. Eventually, 30,000 different photon paths have been considered. The look-up table is utilized by a KD-search [56] and an inverse distance weighted interpolation. This approach is well suited for data that cannot be structured in an hypercube.

The harmonization works as follows. First, the OLCI bands 12–16 are normalized with respect to their corresponding in-band solar irradiance F.

$$I_i^N = \frac{I_i}{F_i}(i = 12, \ldots, 16) \tag{A4}$$

Then, the window bands 12 and 16 are interpolated to the spectral position of the bands 13, 14 and 15, respectively:

$$\tilde{I}_i^N = \frac{I_{16}^N - I_{12}^N}{\lambda_{16} - \lambda_{12}} \cdot (\lambda_i - \lambda_{12})(i = 13, 14, 15) \tag{A5}$$

The apparent transmission is now calculated with

$$t_i = \frac{I_i^N}{\tilde{I}_i^N}(i = 13, 14, 15) \tag{A6}$$

For every pixel and band the sensitivity factor, ξ is searched within in the look-up table, based on the following four quantities: the apparent transmission t_i, the pixel specific central wavelength λ, the bandwidth $FWHM$ and the air mass factor amf.

$$amf = \frac{1}{cos\theta_{VZA}} + \frac{1}{cos\theta_{SZA}} \tag{A7}$$

The look-up table search, as well as the inverse distance weighting, uses normalized quantities, but we refrain from further indexing to maintain clarity.

$$x_{norm} = \frac{x}{x_{max} - x_{min}} \tag{A8}$$

x_{max} and x_{min} are the smallest and largest values of the respective coordinate. The eight closest matches are used to calculate an estimate of ξ by an inverse distance-weighted mean.

$$\xi_i^{pixel} = \frac{1}{\sum_{j=0}^{8} w_i^j} \cdot \sum_{j=0}^{8} w_i^j \cdot \xi_i^j \quad (i = 13, 14, 15) \tag{A9}$$

ξ_i^j is the sensitivity factor of band i of the j closest neighbors. The weight w is the inverse Euclidian distance:

$$w_i^j = \frac{1}{\epsilon + \sqrt{(amf^{pixel} - amf_j)^2 + (\lambda_i^{pixel} - \lambda_i^j)^2 + (FWHM_i^{pixel} - FWHM_i^j)^2 + (t_i^{pixel} - t_i^j)^2}} \tag{A10}$$

ϵ is a small number, preventing division by zero for cases where the closest distance is zero. The final step is the calculation of the apparent transmission at nominal position:

$$t_i^{nominal} = \frac{t_i}{\xi_i^{pixel}}(i = 13, 14, 15) \tag{A11}$$

Appendix C. Sensitivity Study for Glint Scene

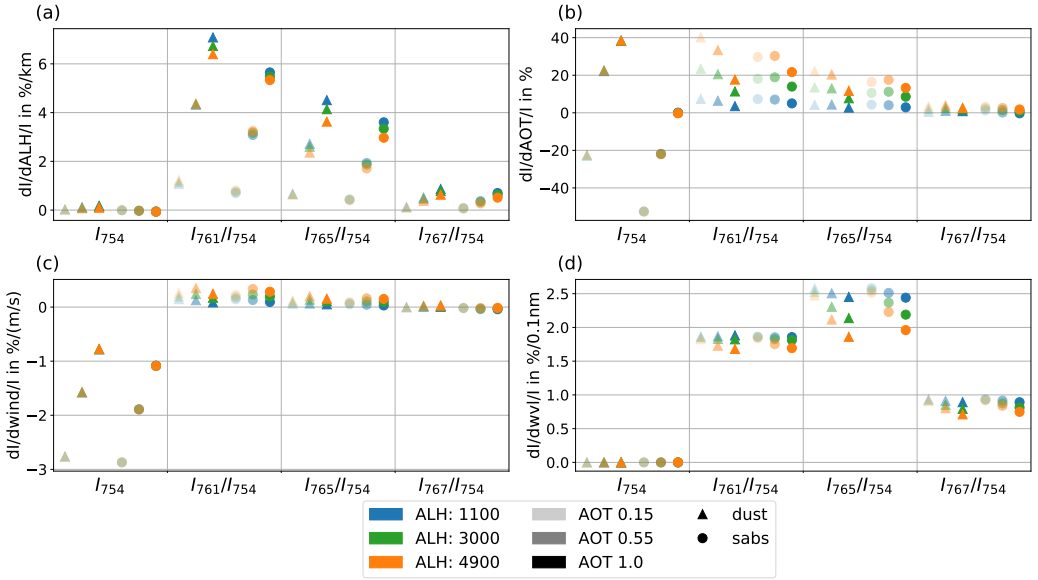

Figure A1. Jacobians of TOA radiance ratios at different central wavelengths relative to the ALH, AOT, wind speed and central wavelength. Jacobians are given for two aerosol models (circles: strong absorbing, triangles: dust) and for different AOTs (transparent: 0.15, non-transparent: 1.0). All results are given for SZA of 30°, VZA at 46° and AZI at 10° (**a**–**d**).

Appendix D. Sun Glint Geometry for Test Scenes

Both test scenes are over ocean surfaces under cloud-free conditions. Under certain sun and observation geometries, sun light is strongly backscattered by the ocean surface. The size of this area depends on the surface roughness and thus the wind speed. This area is called sun glint. OLCI's L1 data includes a sun glint risk flag, which is presented in Figure A2a for the dust test scene and in Figure A3a for the SABS scene. The congruent sun and observation angles are shown in Figures A2b–d and A3b–d.

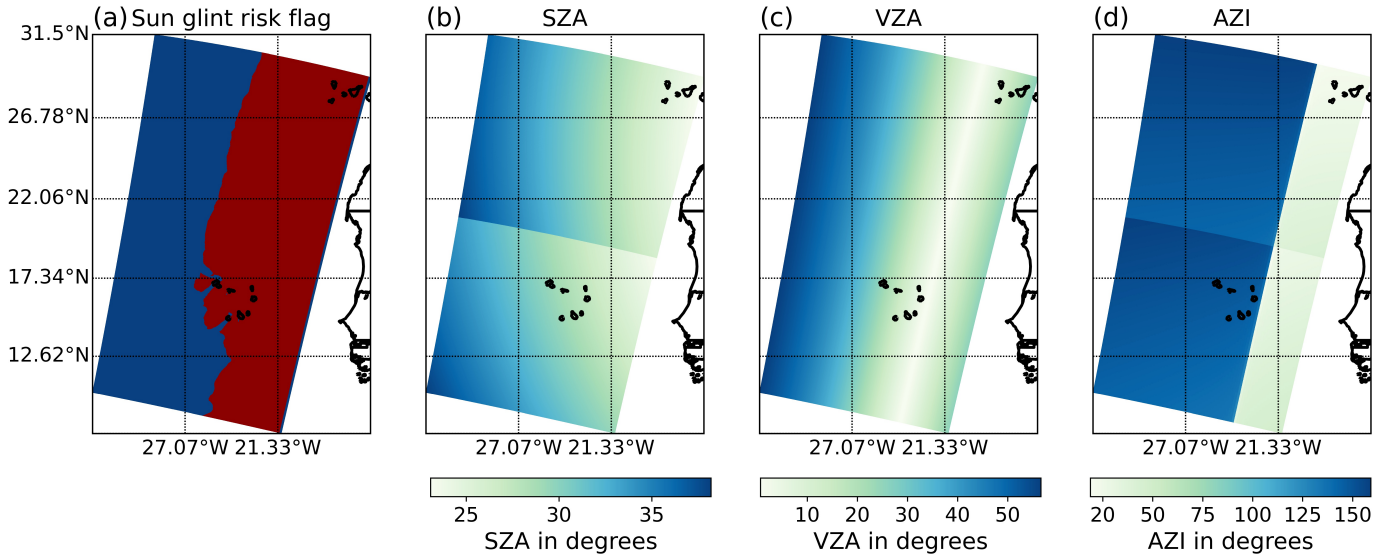

Figure A2. (**a**) Sun glint risk flag for dust test case on 18/06/2020 at the west coast of Africa. For the red pixels, the sun glint risk is true, and for blue pixels, it is false. (**b**) SZA in degrees for the two OLCI-B sequences. (**c**,**d**) VZA and AZI in degrees for the two OLCI-B sequences, respectively.

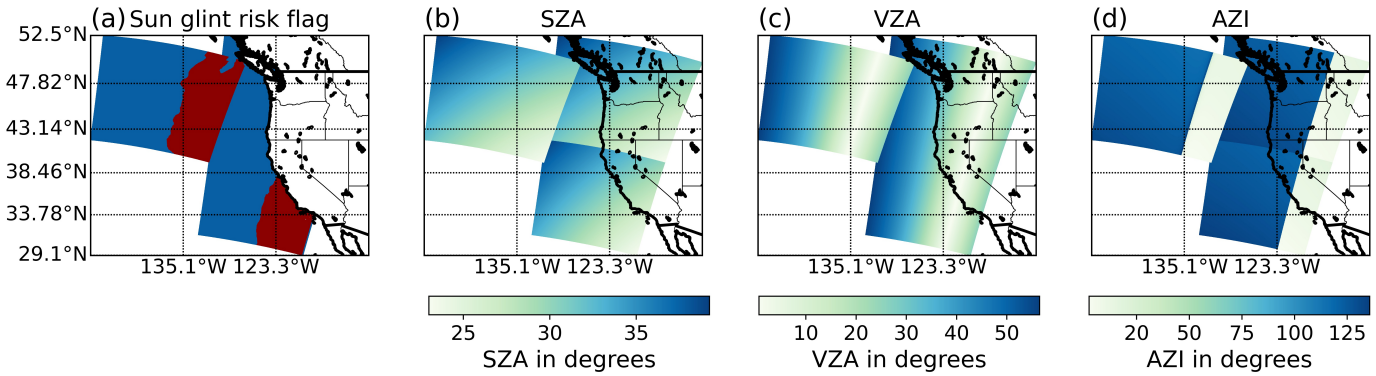

Figure A3. (**a**) Sun glint risk flag for dust test case on 08/09/2020 at the west coast of North America. For the red pixels, the sun glint risk is true, and for blue pixels, it is false. (**b**) SZA in degrees for the OLCI-A and OLCI-B sequences. (**c**,**d**) VZA and AZI in degrees for the OLCI-A and OLCI-B sequences, respectively.

Appendix E. Uncertainty of ALH Depending on AOT

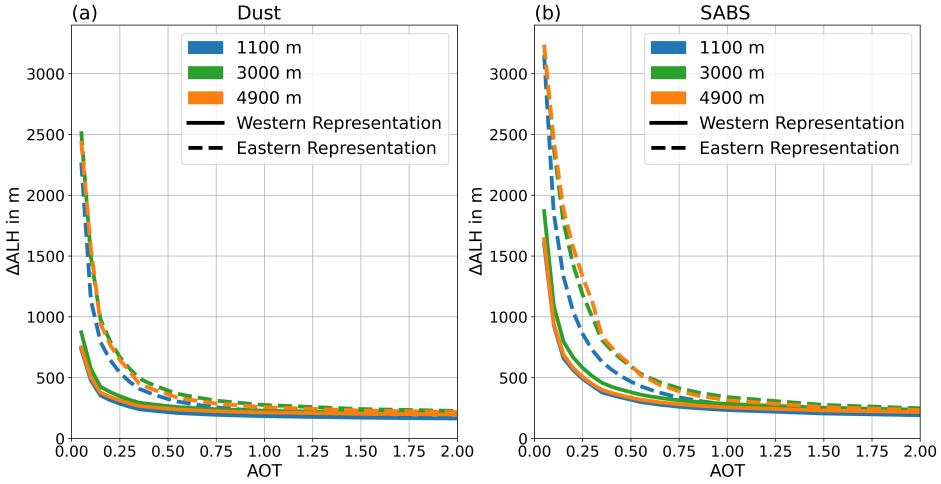

Figure A4. Uncertainty of ALH from retrieval error covariance matrix over AOT for different simulated dust cases (**a**) and SABS cases (**b**) with observation geometries of (i) the western representation (solid lines): SZA of 40°, VZA at 50° and AZI at 150° and (ii) the eastern representation (dashed lines): SZA of 40°, VZA at 25° and AZI at 40°. The colors show simulations with different ALHs: blue: 1100 m; green: 3000 m and orange: 4900 m.

The uncertainty of ALH is studied with respect to AOT. We simulated cases with dust and SABS particles for different observation geometries which are representative for the geometries at the western and eastern border of the S3A and S3B sequences. The SZA was chosen according to the test scene over the west coast of north America on 08/09/2020 (Figure 7). The eastern geometries are a SZA of 40°, a VZA at 50° and an AZI at 150°, and the western geometries are a SZA of 40°, a VZA at 25° and an AZI at 40°. We calculated the retrieval error covariance matrix (Equation (6)), which includes uncertainty of the retrieval parameter ALH and AOT. To include the same uncertainty for the wind speed of 1 m/s as assumed in Section 4.1, we simulated the effect of the wind speed change of 1 m/s. The simulation was used to calculate corresponding uncertainty, which is added to the radiance uncertainty.

In all cases, the uncertainty of theALH decreases with the AOT with a saturation at an AOT of about 1. For AOTs larger than 0.55, all uncertainties are below 500 m. The ALH uncertainty is similar for aerosol at different heights. The eastern, glint-influenced simulations show a larger uncertainty than the western ones. Both geometries differ in

the scattering direction of the aerosol, while the western geometry is pointed in the back scattering direction and the eastern in the forward scattering direction. Additionally, the sun glint effects only the eastern simulations, which increases the ALH uncertainty further.

References

1. Xu, X.; Wang, J.; Wang, Y.; Kokhanovsky, A. Passive remote sensing of aerosol height. In *Remote Sensing of Aerosols, Clouds, and Precipitation*; Elsevier: Amsterdam, The Netherlands, 2018; pp. 1–22.
2. Kylling, A.; Vandenbussche, S.; Capelle, V.; Cuesta, J.; Klüser, L.; Lelli, L.; Popp, T.; Stebel, K.; Veefkind, P. Comparison of dust-layer heights from active and passive satellite sensors. *Atmos. Meas. Tech.* **2018**, *11*, 2911–2936.
3. Kipling, Z.; Stier, P.; Johnson, C.E.; Mann, G.W.; Bellouin, N.; Bauer, S.E.; Bergman, T.; Chin, M.; Diehl, T.; Ghan, S.J.; et al. What controls the vertical distribution of aerosol? Relationships between process sensitivity in HadGEM3–UKCA and inter-model variation from AeroCom Phase II. *Atmos. Chem. Phys.* **2016**, *16*, 2221–2241. [CrossRef]
4. Pachauri, R.K.; Allen, M.R.; Barros, V.R.; Broome, J.; Cramer, W.; Christ, R.; Church, J.A.; Clarke, L.; Dahe, Q.; Dasgupta, P.; et al. *Climate Change 2014: Synthesis Report. Contribution of Working Groups I, II and III to the Fifth Assessment Report of the Intergovernmental Panel on Climate Change*; IPCC: Geneva, Switzerland, 2014.
5. Colosimo, S.F.; Natraj, V.; Sander, S.P.; Stutz, J. A sensitivity study on the retrieval of aerosol vertical profiles using the oxygen A-band. *Atmos. Meas. Tech.* **2016**, *9*, 1889–1905. [CrossRef]
6. Copernicus. Record-Breaking North Atlantic Ocean Temperatures Contribute to Extreme Marine Heatwaves. Available online: https://climate.copernicus.eu/record-breaking-north-atlantic-ocean-temperatures-contribute-extreme-marine-heatwaves (accessed on 2 August 2023).
7. Houweling, S.; Hartmann, W.; Aben, I.; Schrijver, H.; Skidmore, J.; Roelofs, G.J.; Breon, F.M. Evidence of systematic errors in SCIAMACHY-observed CO_2 due to aerosols. *Atmos. Chem. Phys.* **2005**, *5*, 3003–3013. [CrossRef]
8. Guerlet, S.; Butz, A.; Schepers, D.; Basu, S.; Hasekamp, O.; Kuze, A.; Yokota, T.; Blavier, J.F.; Deutscher, N.; Griffith, D.T.; et al. Impact of aerosol and thin cirrus on retrieving and validating XCO_2 from GOSAT shortwave infrared measurements. *J. Geophys. Res. Atmos.* **2013**, *118*, 4887–4905. [CrossRef]
9. Chimot, J.; Veefkind, J.P.; De Haan, J.F.; Stammes, P.; Levelt, P.F. Minimizing aerosol effects on the OMI tropospheric NO_2 retrieval–An improved use of the 477 nm O_2-O_2 band and an estimation of the aerosol correction uncertainty. *Atmos. Meas. Tech.* **2019**, *12*, 491–516. [CrossRef]
10. Torres, O.; Ahn, C.; Chen, Z. Improvements to the OMI near UV aerosol algorithm using A-train CALIOP and AIRS observations. *Atmos. Meas. Tech. Discuss.* **2013**, *6*, 5621–5652. [CrossRef]
11. Li, C.; Li, J.; Dubovik, O.; Zeng, Z.C.; Yung, Y.L. Impact of Aerosol Vertical Distribution on Aerosol Optical Depth Retrieval from Passive Satellite Sensors. *Remote Sens.* **2020**, *12*, 1524. [CrossRef]
12. Frankenberg, C.; Butz, A.; Toon, G.C. Disentangling chlorophyll fluorescence from atmospheric scattering effects in O_2 A-band spectra of reflected sun-light. *Geophys. Res. Lett.* **2011**, *38*. [CrossRef]
13. Duforêt, L.; Frouin, R.; Dubuisson, P. Importance and estimation of aerosol vertical structure in satellite ocean-color remote sensing. *Appl. Opt.* **2007**, *46*, 1107–1119. [CrossRef]
14. Winker, D.M.; Vaughan, M.A.; Omar, A.; Hu, Y.; Powell, K.A.; Liu, Z.; Hunt, W.H.; Young, S.A. Overview of the CALIPSO Mission and CALIOP Data Processing Algorithms. *J. Atmos. Ocean. Technol.* **2009**, *26*, 2310–2323. [CrossRef]
15. Kokhanovsky, A.A.; Rozanov, V.V. The determination of dust cloud altitudes from a satellite using hyperspectral measurements in the gaseous absorption band. *Int. J. Remote Sens.* **2010**, *31*, 2729–2744. [CrossRef]
16. Hollstein, A.; Fischer, J. Retrieving aerosol height from the oxygen A band: A fast forward operator and sensitivity study concerning spectral resolution, instrumental noise, and surface inhomogeneity. *Atmos. Meas. Tech.* **2014**, *7*, 1429–1441. [CrossRef]
17. Dubuisson, P.; Frouin, R.; Dessailly, D.; Duforêt, L.; Léon, J.F.; Voss, K.; Antoine, D. Estimating the altitude of aerosol plumes over the ocean from reflectance ratio measurements in the O_2 A-band. *Remote Sens. Environ.* **2009**, *113*, 1899–1911. [CrossRef]
18. Preusker, R.; Lindstrot, R. Remote sensing of cloud-top pressure using moderately resolved measurements within the oxygen A band—A sensitivity study. *J. Appl. Meteorol. Climatol.* **2009**, *48*, 1562–1574. [CrossRef]
19. Sanghavi, S.; Martonchik, J.; Landgraf, J.; Platt, U. Retrieval of the optical depth and vertical distribution of particulate scatterers in the atmosphere using O_2 A-and B-band SCIAMACHY observations over Kanpur: A case study. *Atmos. Meas. Tech.* **2012**, *5*, 1099–1119. [CrossRef]
20. Nanda, S.; Veefkind, J.P.; De Graaf, M.; Sneep, M.; Stammes, P.; De Haan, J.F.; Sanders, A.F.; Apituley, A.; Tuinder, O.; Levelt, P.F. A weighted least squares approach to retrieve aerosol layer height over bright surfaces applied to GOME-2 measurements of the oxygen A band for forest fire cases over Europe. *Atmos. Meas. Tech.* **2018**, *11*, 3263–3280. [CrossRef]
21. Zeng, Z.C.; Chen, S.; Natraj, V.; Le, T.; Xu, F.; Merrelli, A.; Crisp, D.; Sander, S.P.; Yung, Y.L. Constraining the vertical distribution of coastal dust aerosol using OCO-2 O2 A-band measurements. *Remote Sens. Environ.* **2020**, *236*, 111494. [CrossRef]
22. Nanda, S.; De Graaf, M.; Veefkind, J.P.; Ter Linden, M.; Sneep, M.; De Haan, J.; Levelt, P.F. A neural network radiative transfer model approach applied to the Tropospheric Monitoring Instrument aerosol height algorithm. *Atmos. Meas. Tech.* **2019**, *12*, 6619–6634. [CrossRef]

23. Werdell, P.J.; Behrenfeld, M.J.; Bontempi, P.S.; Boss, E.; Cairns, B.; Davis, G.T.; Franz, B.A.; Gliese, U.B.; Gorman, E.T.; Hasekamp, O.; et al. The Plankton, Aerosol, Cloud, Ocean Ecosystem Mission: Status, Science, Advances. *Bull. Am. Meteorol. Soc.* **2019**, *100*, 1775–1794. [CrossRef]
24. Remer, L.A.; Davis, A.B.; Mattoo, S.; Levy, R.C.; Kalashnikova, O.V.; Coddington, O.; Chowdhary, J.; Knobelspiesse, K.; Xu, X.; Ahmad, Z.; et al. Retrieving aerosol characteristics from the PACE mission, Part 1: Ocean Color Instrument. *Front. Earth Sci.* **2019**, *7*, 152. [CrossRef]
25. Xu, X.; Wang, J.; Wang, Y.; Zeng, J.; Torres, O.; Reid, J.S.; Miller, S.D.; Martins, J.V.; Remer, L.A. Detecting layer height of smoke aerosols over vegetated land and water surfaces via oxygen absorption bands: Hourly results from EPIC/DSCOVR in deep space. *Atmos. Meas. Tech.* **2019**, *12*, 3269–3288. [CrossRef]
26. Chimot, J.; Veefkind, J.P.; Vlemmix, T.; de Haan, J.F.; Amiridis, V.; Proestakis, E.; Marinou, E.; Levelt, P.F. An exploratory study on the aerosol height retrieval from OMI measurements of the 477 nm O_2 O_2 spectral band using a neural network approach. *Atmos. Meas. Tech.* **2017**, *10*, 783–809. [CrossRef]
27. Donlon, C.; Berruti, B.; Buongiorno, A.; Ferreira, M.H.; Féménias, P.; Frerick, J.; Goryl, P.; Klein, U.; Laur, H.; Mavrocordatos, C. The global monitoring for environment and security (GMES) sentinel-3 mission. *Remote Sens. Environ.* **2012**, *120*, 37–57. [CrossRef]
28. Hollstein, A.; Fischer, J. Radiative transfer solutions for coupled atmosphere ocean systems using the matrix operator technique. *J. Quant. Spectrosc. Radiat. Transf.* **2012**, *113*, 536–548. [CrossRef]
29. Fell, F.; Fischer, J. Numerical simulation of the light field in the atmosphere–ocean system using the matrix-operator method. *J. Quant. Spectrosc. Radiat. Transf.* **2001**, *69*, 351–388. [CrossRef]
30. Cox, C.; Munk, W. Measurement of the roughness of the sea surface from photographs of the sun's glitter. *Josa* **1954**, *44*, 838–850. [CrossRef]
31. Doppler, L.; Preusker, R.; Bennartz, R.; Fischer, J. k-bin and k-IR: K-distribution methods without correlation approximation for non-fixed instrument response function and extension to the thermal infrared—Applications to satellite remote sensing. *J. Quant. Spectrosc. Radiat. Transf.* **2014**, *133*, 382–395. [CrossRef]
32. Gordon, I.; Rothman, L.; Hill, C.; Kochanov, R.; Tan, Y.; Bernath, P.; Birk, M.; Boudon, V.; Campargue, A.; Chance, K.; et al. The HITRAN2016 molecular spectroscopic database. *J. Quant. Spectrosc. Radiat. Transf.* **2017**, *203*, 3–69. [CrossRef]
33. Drouin, B.J.; Benner, D.C.; Brown, L.R.; Cich, M.J.; Crawford, T.J.; Devi, V.M.; Guillaume, A.; Hodges, J.T.; Mlawer, E.J.; Robichaud, D.J. Multispectrum analysis of the oxygen A-band. *J. Quant. Spectrosc. Radiat. Transf.* **2017**, *186*, 118–138. [CrossRef]
34. Anderson, G.P.; Clough, S.A.; Kneizys, F.X.; Chetwynd, J.H.; Shettle, E.P. AFGL Atmospheric Constituent Profiles (0.120 km). Technical Report AFGL-TR-86-0110, AIR FORCE GEOPHYSICS LAB HANSCOM AFB MA. 1986. Available online: https://apps.dtic.mil/docs/citations/ADA175173 (accessed on 5 September 2022).
35. Dubovik, O.; Sinyuk, A.; Lapyonok, T.; Holben, B.N.; Mishchenko, M.; Yang, P.; Eck, T.F.; Volten, H.; Muñoz, O.; Veihelmann, B.; et al. Application of spheroid models to account for aerosol particle nonsphericity in remote sensing of desert dust. *J. Geophys. Res. Atmos.* **2006**, *111*, 6619. [CrossRef]
36. Wandinger, U.; Floutsi, A.A.; Baars, H.; Haarig, M.; Ansmann, A.; Hünerbein, A.; Docter, N.; Donovan, D.; van Zadelhoff, G.J.; Mason, S.; et al. HETEAC–The Hybrid End-To-End Aerosol Classification model for EarthCARE. *Atmos. Meas. Tech.* **2023**, *16*, 2485–2510. [CrossRef]
37. Liou, K.N. *An Introduction to Atmospheric Radiation*; Elsevier: Amsterdam, The Netherlands, 2002; Volume 84, p. 528.
38. Wiscombe, W.J. Improved Mie scattering algorithms. *Appl. Opt.* **1980**, *19*, 1505–1509. [CrossRef]
39. Preusker, R. Sentinel-3 OLCI Temporal Model of Spectral Characteristics. 2021. Available online: https://sentinel.esa.int/documents/247904/2700436/S3MPC_OLCI_spectral_characterisation_SD_RP_EUM_SD_v1.1.pdf (accessed on 3 July 2023).
40. Preusker, R. SNAP Data Processors-OLCI O2A Harmonisation Algorithm Specification. Available online: https://seadas.gsfc.nasa.gov/help-8.3.0/harmonisation/OlciO2aHarmonisationAlgorithmSpecification.html (accessed on 3 July 2023).
41. Preusker, R.; Fischer, J. Study on the Cloud Top Pressure Development from Snetinel-3 OLCI OCTPO2-Algorithm Theoretical Basis Document (ATBD). Technical Report, EUMETSAT. 2021. Available online: https://www-cdn.eumetsat.int/files/2021-09/OCTPO2_ATBD_CTP_v2-2.pdf (accessed on 3 July 2023).
42. Yu, H.; Tan, Q.; Zhou, L.; Zhou, Y.; Bian, H.; Chin, M.; Ryder, C.L.; Levy, R.C.; Pradhan, Y.; Shi, Y.; et al. Observation and modeling of the historic "Godzilla" African dust intrusion into the Caribbean Basin and the southern US in June 2020. *Atmos. Chem. Phys.* **2021**, *21*, 12359–12383. [CrossRef]
43. Veefkind, J.; Aben, I.; McMullan, K.; Förster, H.; de Vries, J.; Otter, G.; Claas, J.; Eskes, H.; de Haan, J.; Kleipool, Q.; et al. TROPOMI on the ESA Sentinel-5 Precursor: A GMES mission for global observations of the atmospheric composition for climate, air quality and ozone layer applications. *Remote Sens. Environ.* **2012**, *120*, 70–83. . [CrossRef]
44. Nanda, S.; de Graaf, M.; Veefkind, J.P.; Sneep, M.; ter Linden, M.; Sun, J.; Levelt, P.F. A first comparison of TROPOMI aerosol layer height (ALH) to CALIOP data. *Atmos. Meas. Tech.* **2020**, *13*, 3043–3059. [CrossRef]
45. Koffi, B.; Schulz, M.; Bréon, F.M.; Griesfeller, J.; Winker, D.; Balkanski, Y.; Bauer, S.; Berntsen, T.; Chin, M.; Collins, W.D.; et al. Application of the CALIOP layer product to evaluate the vertical distribution of aerosols estimated by global models: AeroCom phase I results. *J. Geophys. Res. Atmos.* **2012**, *117*, 16858. [CrossRef]
46. Rodgers, C.D. *Inverse Methods for Atmospheric Sounding: Theory and Practice*; World Scientific: Singapore, 2000; Volume 2.

47. Stein, A.F.; Draxler, R.R.; Rolph, G.D.; Stunder, B.J.B.; Cohen, M.D.; Ngan, F. NOAA's HYSPLIT Atmospheric Transport and Dispersion Modeling System. *Bull. Am. Meteorol. Soc.* **2015**, *96*, 2059–2077. [CrossRef]
48. Menzel, W.P.; Frey, R.A.; Zhang, H.; Wylie, D.P.; Moeller, C.C.; Holz, R.E.; Maddux, B.; Baum, B.A.; Strabala, K.I.; Gumley, L.E. MODIS Global Cloud-Top Pressure and Amount Estimation: Algorithm Description and Results. *J. Appl. Meteorol. Climatol.* **2008**, *47*, 1175–1198. [CrossRef]
49. Morcrette, J.J.; Boucher, O.; Jones, L.; Salmond, D.; Bechtold, P.; Beljaars, A.; Benedetti, A.; Bonet, A.; Kaiser, J.W.; Razinger, M.; et al. Aerosol analysis and forecast in the European Centre for Medium-Range Weather Forecasts Integrated Forecast System: Forward modeling. *J. Geophys. Res. Atmos.* **2009**, *114*, 11235. [CrossRef]
50. Wevers, J.; Müller, D.; Kirches, G.; Quast, R.; Brockmann, C. *IdePix for Sentinel-3 OLCI Algorithm Theoretical Basis Document. Technical Report, Brockmann Consult GMBH*; Zenodo: Vienna, Austria, 2022. [CrossRef]
51. Griffin, D.; Sioris, C.; Chen, J.; Dickson, N.; Kovachik, A.; de Graaf, M.; Nanda, S.; Veefkind, P.; Dammers, E.; McLinden, C.A.; et al. The 2018 fire season in North America as seen by TROPOMI: Aerosol layer height intercomparisons and evaluation of model-derived plume heights. *Atmos. Meas. Tech.* **2020**, *13*, 1427–1445. [CrossRef]
52. Michailidis, K.; Koukouli, M.E.; Balis, D.; Veefkind, J.P.; de Graaf, M.; Mona, L.; Papagianopoulos, N.; Pappalardo, G.; Tsikoudi, I.; Amiridis, V.; et al. Validation of the TROPOMI/S5P aerosol layer height using EARLINET lidars. *Atmos. Chem. Phys.* **2023**, *23*, 1919–1940. [CrossRef]
53. Chen, X.; Wang, J.; Xu, X.; Zhou, M.; Zhang, H.; Castro Garcia, L.; Colarco, P.R.; Janz, S.J.; Yorks, J.; McGill, M.; et al. First retrieval of absorbing aerosol height over dark target using TROPOMI oxygen B band: Algorithm development and application for surface particulate matter estimates. *Remote Sens. Environ.* **2021**, *265*, 112674. [CrossRef]
54. Peuch, V.H.; Engelen, R.; Rixen, M.; Dee, D.; Flemming, J.; Suttie, M.; Ades, M.; Agustí-Panareda, A.; Ananasso, C.; Andersson, E.; et al. The Copernicus Atmosphere Monitoring Service: From Research to Operations. *Bull. Am. Meteorol. Soc.* **2022**, *103*, E2650–E2668. [CrossRef]
55. Kokhanovsky, A.A.; Leeuw, G. *Satellite Aerosol Remote Sensing over Land*; Springer: Berlin/Heidelberg, Germany, 2009; Volume 111, p. 24.
56. Bentley, J.L. Multidimensional binary search trees used for associative searching. *Commun. ACM* **1975**, *18*, 509–517. [CrossRef]